

Two-Dimensional Metal Oxide Nanosheets as Building Blocks for Artificial Photosynthetic Assemblies

Kazuhiko Maeda*¹ and Thomas E. Mallouk²

¹Department of Chemistry, School of Science, Tokyo Institute of Technology, 2-12-1-NE-2 Ookayama, Meguro-ku, Tokyo 152-8550, Japan

²Departments of Chemistry, Biochemistry and Molecular Biology, and Physics, The Pennsylvania State University, University Park, Pennsylvania 16802, USA

E-mail: maedak@chem.titech.ac.jp

Received: September 4, 2018; Accepted: September 18, 2018; Web Released: October 4, 2018



Kazuhiko Maeda

Kazuhiko Maeda received his PhD from The University of Tokyo (2007) under the supervision of Professor Kazunari Domen. During 2008–2009, he was a postdoctoral fellow at Pennsylvania State University where he worked with Professor Thomas E. Mallouk. In 2009, he joined The University of Tokyo as an Assistant Professor. Moving to Tokyo Institute of Technology in 2012, he was promoted to an Associate Professor. During 2010–2014, he was appointed as a research fellow of the PRESTO/JST program (Chemical Conversion of Light Energy). His research interests include water splitting and CO₂ reduction using semiconductor materials as photocatalysts and photoelectrodes.



Thomas E. Mallouk

Thomas E. Mallouk received his Sc.B. degree from Brown University (1977) and his Ph.D. in Chemistry from the University of California, Berkeley (1983). He was a postdoctoral fellow at Massachusetts Institute of Technology (1983–1985). His research focuses on the synthesis, assembly, and applications of nanoscale inorganic materials.

Abstract

Two-dimensional metal oxide nanosheets are versatile materials for constructing artificial photosynthetic systems that can carry out photocatalytic processes such as water splitting and CO₂ fixation. Nanosheets are anisotropic single-crystals that have thicknesses of 1–2 nm and lateral dimensions ranging from several hundreds of nanometers to a few micrometers. This structural feature is advantageous for use as heterogeneous photocatalysts, because the diffusion length of photogenerated electron/hole pairs to the surface can be shortened, with less probability of electron/hole recombination. In this Account, recent progress on the development of metal oxide nanosheets and related materials for applications in photocatalytic water splitting and CO₂ fixation made by the authors' groups is described.

Keywords: Heterogeneous photocatalysis | Solar energy conversion | Dye-sensitization

1. Introduction

1.1 Research Background. In recent years, the development of semiconductor photocatalysts that can convert solar energy into stored chemical energy has attracted considerable attention due to the increasing demand for renewable energy.^{1–10} Water splitting and CO₂ fixation are the most popular reactions among artificial photosynthetic schemes, and various semiconductors have been studied to date as components of these systems. Recent techno-economic analyses suggest that systems with high quantum yield and good stability could be practical for conversion of solar energy to fuel.¹¹ However, a satisfactory system has not been devised so far.

In semiconductor-based photocatalytic reactions, electrons in the valence band of the semiconductor are excited into the

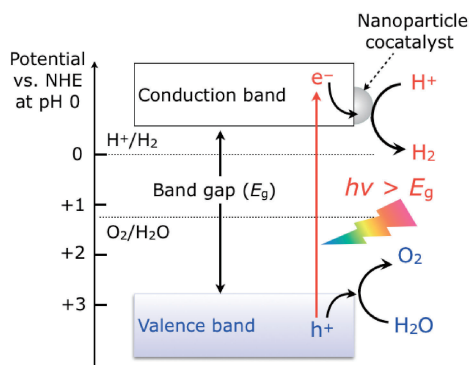


Figure 1. Basic principle of overall water splitting using a semiconductor photocatalyst. E_g denotes the band gap energy of the semiconductor.

conduction band after absorbing light of energy greater than the band gap. The resulting holes in the valence band and electrons in the conduction band can cause oxidation and reduction reactions, respectively. Taking the overall water splitting reaction as an example (Figure 1), the conduction band minimum has to be located at a more negative potential than the water reduction potential so as to drive proton reduction to form H_2 . On the other hand, the valence band maximum should lie at a position more positive than the water oxidation potential.

In addition to the thermodynamic requirements to split pure water into H_2 and O_2 , electron/hole recombination needs to be minimized in order to maximize the quantum yield of surface chemical reactions. To do this, nanoparticulate cocatalysts (typically noble metals or metal oxides) are loaded onto the semiconductor surface to construct active sites (in most cases, for water reduction) and reduce the activation energy for the reaction.

Increasing the crystallinity and surface area is another important point for enhancing the photocatalytic activity of a semiconductor. High crystallinity reduces structural defects and/or vacancies, which can act as recombination sites for electrons and holes, in a semiconductor. Larger surface area gives a greater number of reaction sites, thereby promoting surface redox reactions. However, it is difficult for an ordinary “bulk-type” photocatalyst to satisfy both high crystallinity and high surface area. In general, high temperature is required to synthesize a highly crystallized photocatalyst, while specific surface area becomes smaller by crystal growth that occurs at higher temperatures. On the other hand, although a low calcination temperature should increase the specific surface area, it also generally leads to lower crystallinity.

1.2 Key Features of Nanosheets as Photocatalysts.

Certain layered metal oxides undergo exfoliation by reaction with a bulky organic base such as tetra(*n*-butyl)ammonium hydroxide (TBA^+OH^-), producing unilamellar single crystalline colloidal sheets having a thickness of 1–2 nm, which are called “nanosheets”.^{12–14} Metal oxide nanosheets have been studied as functional materials including photocatalysts, solid-acid catalysts, phosphors, catalyst supports, and so on.^{4,15–19} As shown in Figure 2, metal oxide nanosheets have several features that are advantageous for photocatalytic applications, compared with analogous three dimensionally bonded materi-

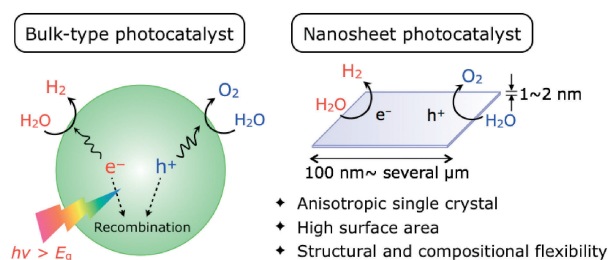


Figure 2. Comparison of bulk-type particles and nanosheets as photocatalysts.

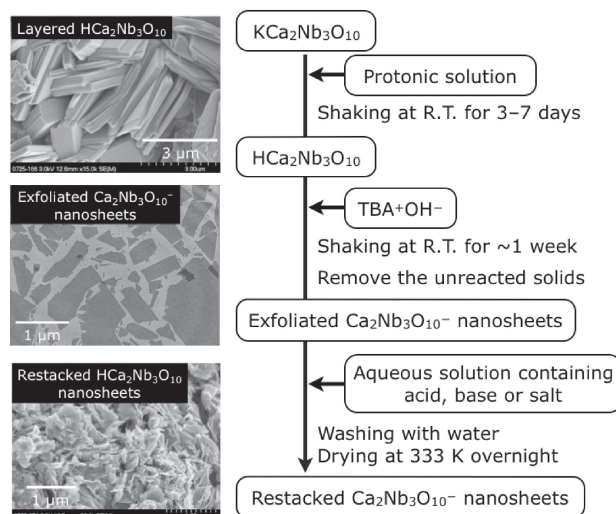


Figure 3. A typical procedure for proton-exchange, exfoliation and restacking of $KCa_2Nb_3O_{10}$, along with SEM and TEM images. Images are reproduced from Ref. 42 with permission from The Royal Society of Chemistry.

als. First, both high crystallinity and large surface area can be realized, as nanosheets are typically single-crystalline and have an extremely high surface-area-to-volume ratio. Second, the nanoscale thickness is beneficial for migration of photogenerated charge carriers to the surface, which reduces the possibility of electron/hole recombination, leading to higher activity. Besides, nanosheets can be used as building blocks to construct multicomponent photosystems that incorporate electron donors/acceptors, nanoparticle catalysts, or organic molecules such as dye-sensitizers,^{4,17,18,20–24} because of their high surface area and the wide variety of compositions available.

1.3 Synthesis of Metal Oxide Nanosheets. Figure 3 shows a typical procedure for the synthesis of metal oxide nanosheets, taking the Dion-Jacobson type layer perovskite $HCa_2Nb_3O_{10}$ as an example. First, an ion-exchangeable layered metal oxide (here $KCa_2Nb_3O_{10}$), which was first synthesized by an appropriate method such as a solid-state reaction (SSR) or the polymerized complex (PC) method, is dispersed in acidic aqueous solution to replace exchangeable cations in the interlayer galleries of the parent layered solid with H^+ . The protonated layered metal oxide, $HCa_2Nb_3O_{10}$, is then reacted with TBA^+OH^- , and the bulky TBA^+ cation is intercalated and exfoliates the layer, ultimately yielding a suspension of unilamellar nanosheets. The exfoliated $TBA_xH_{1-x}Ca_2Nb_3O_{10}$ ($x \approx 0.25$) nanosheets, hereafter denoted as “ $Ca_2Nb_3O_{10}^-$ ” can be restacked upon

addition of acid, base or salt into the suspension. The aggregated nanosheets are usually used for photocatalytic applications, as they are in an easy-to-handle form. Through the exfoliation-restacking process, the ordered lamellar structure of the parent solid is completely lost, producing highly disordered aggregates with high specific surface area.

1.4 Scope of this Account. Domen et al. pioneered layered metal oxides as efficient photocatalysts for overall water splitting in the 1980s.^{25,26} This discovery triggered research on various layered metal oxides as photocatalysts.^{3,6} In the early 2000s, restacked $\text{Ca}_2\text{Nb}_3\text{O}_{10}^-$ nanosheets were reported as new photocatalysts for H_2 evolution from a water-methanol mixture, which could work more efficiently than the host layered solid.^{20,21} Osterloh et al. studied photocatalytic properties of individual nanosheets of $\text{Ca}_2\text{Nb}_3\text{O}_{10}^-$.^{27–31} Ida et al. reported that Rh-doped $\text{Ca}_2\text{Nb}_3\text{O}_{10}^-$ nanosheets showed much higher activity for H_2 evolution than their unexfoliated layered counterparts.³² Following these early studies, titanate, titanoniobate and tungstate nanosheets were reported as well.^{33,34} The general conclusion of these works is that “nanosheet is better than bulk”, in line with the expectations implied in Figure 2. However, the photocatalytic properties of metal oxide nanosheets (e.g., in terms of size effects, compositional effects, and so on) had not been investigated in detail, in contrast to bulk-type metal oxides that had been extensively studied. It should be also noted that most metal oxide nanosheets are responsive only to UV light (<400 nm), because of their large band gaps. To realize the efficient solar energy conversion that is the ultimate goal of the artificial photosynthesis community, it is necessary to develop a visible-light-responsive nanosheet material.

In this Account, the development of metal oxide nanosheet-based photocatalysts for water splitting is described, focusing on recent studies made by the authors' groups over the past 10 years. First, the photocatalytic properties of nanosheets are discussed with regard to their physicochemical properties (e.g., lateral size and composition) using the half reactions of H_2 and O_2 evolution, which are conventionally used as test reactions for overall water splitting.^{2,3,6} Then the key to achieving overall water splitting is discussed, with a focus on restacked $\text{KCa}_2\text{Nb}_3\text{O}_{10}$ nanosheets. In the second half of this Account, visible-light-responsive photocatalytic systems using metal oxide nanosheets and related materials for not only water splitting but also for CO_2 fixation are presented.

2. Oxide Nanosheets as UV-Driven Photocatalysts

2.1 H_2 Evolution Activity. $\text{KCa}_2\text{Nb}_3\text{O}_{10}$ is a Dion-Jacobson type layered perovskite, which has been one of the most studied materials as the parent solid of nanosheet photocatalysts. $\text{KCa}_2\text{Nb}_3\text{O}_{10}$ consists of negatively charged calcium niobate ($\text{Ca}_2\text{Nb}_3\text{O}_{10}^-$) sheets that stack along the b axis to form a two-dimensional layered structure, in which K^+ cations are located between the triple perovskite layers (Figure 4). In $\text{Ca}_2\text{Nb}_3\text{O}_{10}^-$ sheets, niobium (B site) is surrounded by six oxygen atoms to form octahedral units, while Ca occupies the A sites of the perovskite slabs. In this section, studies of nanosheet photocatalysts based on $\text{KCa}_2\text{Nb}_3\text{O}_{10}$ are described.

2.1.1 Effect of Nanosheet Size: It is known that in heterogeneous photocatalysis, the particle size of bulk type

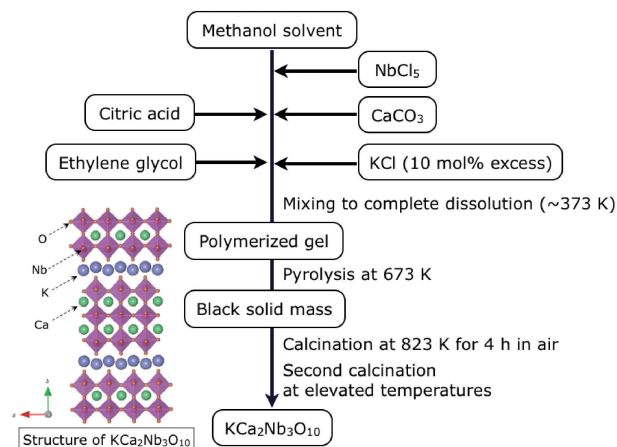


Figure 4. A typical procedure of the polymerized complex method. In the case of $\text{KCa}_2\text{Nb}_3\text{O}_{10}$, an excess amount of KCl is added to compensate the loss from volatilization at high temperatures.

photocatalysts (e.g., TiO_2) has a significant impact on the photocatalytic activity.^{3,6} The size effect of nanosheets was first examined using $\text{HCa}_2\text{Nb}_3\text{O}_{10}$, which was prepared by proton-exchange of $\text{KCa}_2\text{Nb}_3\text{O}_{10}$.³⁵ The layered $\text{KCa}_2\text{Nb}_3\text{O}_{10}$ was synthesized by the PC method.³⁶ As shown in Figure 4, this method consists of two essential steps: (1) incorporation of metal cations into a polymer resin with molecular-level dispersion and (2) subsequent calcination to remove the polymer and to produce a crystalline metal oxide. The lateral size of the nanosheets could be controlled by simply changing the final calcination temperature in the PC synthesis of the host $\text{KCa}_2\text{Nb}_3\text{O}_{10}$, although precise size control to realize narrow size distributions was difficult. Figure 5A shows TEM images of TBA^+ -exfoliated $\text{Ca}_2\text{Nb}_3\text{O}_{10}^-$ nanosheets, which were prepared from layered $\text{KCa}_2\text{Nb}_3\text{O}_{10}$ synthesized at different temperatures. The lateral dimensions of the $\text{Ca}_2\text{Nb}_3\text{O}_{10}^-$ nanosheets tend to increase with increasing temperature. By adding aqueous HCl to the nanosheet suspension, restacked $\text{HCa}_2\text{Nb}_3\text{O}_{10}$ nanosheets were obtained. Specific surface areas of the as-prepared restacked nanosheets, as determined by nitrogen adsorption at 77 K, ranged from 40 to $70 \text{ m}^2 \text{ g}^{-1}$, and higher calcination temperature in the synthesis led to lower specific surface area. The band gaps of the as-synthesized restacked nanosheets were estimated to be ca. 3.5 eV, from the onset wavelength of UV-visible diffuse reflectance spectra (DRS).

Using restacked $\text{HCa}_2\text{Nb}_3\text{O}_{10}$ nanosheets, photocatalytic H_2 evolution activity was investigated under UV irradiation ($\lambda > 300 \text{ nm}$), where the restacked $\text{HCa}_2\text{Nb}_3\text{O}_{10}$ nanosheets underwent photoexcitation. Prior to the reaction, Pt nanoparticles were deposited on the external surface of the restacked nanosheets as cocatalysts for H_2 evolution, and methanol was employed as a sacrificial electron donor. The rate of H_2 evolution on Pt-loaded restacked $\text{HCa}_2\text{Nb}_3\text{O}_{10}$ nanosheets increased with increasing calcination temperature, reaching a maximum at 1273 K and then decreasing (Figure 5B). This behavior can be explained in terms of the crystallinity and specific surface area. The photogenerated electron/hole pairs in the restacked $\text{HCa}_2\text{Nb}_3\text{O}_{10}$ nanosheets have to migrate in the two-dimensional $\text{Ca}_2\text{Nb}_3\text{O}_{10}^-$ sheets without recombination to the

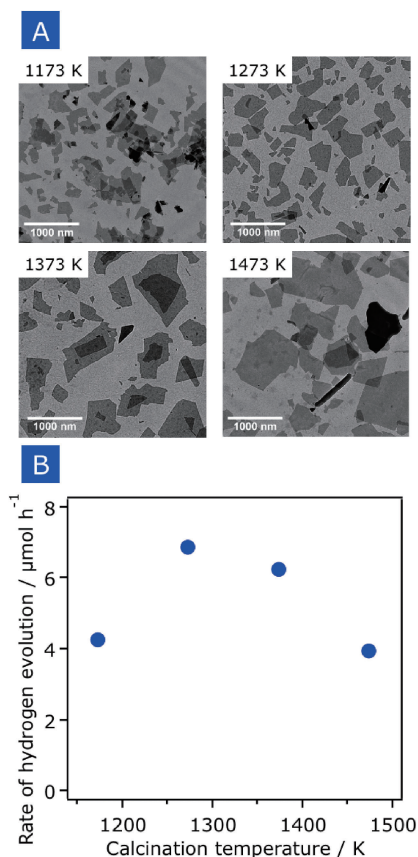


Figure 5. (A) TEM images of exfoliated $\text{TBA}_x\text{H}_{1-x}\text{Ca}_2\text{-Nb}_3\text{O}_{10}$ derived from layered $\text{KCa}_2\text{Nb}_3\text{O}_{10}$ calcined at different temperatures and (B) the rate of H_2 evolution from an aqueous methanol solution using 0.3 wt% Pt-loaded restacked $\text{HCa}_2\text{Nb}_3\text{O}_{10}$ nanosheets under band gap irradiation ($\lambda > 300 \text{ nm}$) as a function of calcination temperature of the parent $\text{KCa}_2\text{Nb}_3\text{O}_{10}$. Reaction conditions: catalyst, 5.0 mg; 1 M aqueous methanol solution, 2.0 mL; light source, 300 W xenon lamp. Reproduced from Ref. 35 with permission. Copyright 2009 American Chemical Society.

surface, reducing and oxidizing proton and methanol, respectively. In general, metal oxide photocatalysts having lower crystallinity, which are typically synthesized by lower temperature calcination, show lower photocatalytic activity, because such oxides contain structural imperfections and/or crystal defects to a large extent.⁶ The enhanced activity observed from 1173 to 1273 K can be therefore explained in terms of the improved crystallinity of the $\text{HCa}_2\text{Nb}_3\text{O}_{10}$ nanosheets. On the other hand, lower specific surface area materials provide a smaller number of reaction sites, which are disadvantageous for surface redox reactions. As mentioned earlier, the specific surface area of the restacked $\text{HCa}_2\text{Nb}_3\text{O}_{10}$ nanosheets decreased with an increase in calcination temperature. The decrease in activity observed at 1373 and 1473 K is most likely a result of the loss of specific surface area, despite higher crystallinity of the nanosheets.

This work also showed that the PC method could give more active photocatalysts with restacked $\text{HCa}_2\text{Nb}_3\text{O}_{10}$ nanosheets than the SSR method, even though the specific surface areas of

the two were almost the same.³⁵ The improved activity of the PC sample is presumably due to lower density of structural imperfections and/or defects in the material. It has been proposed that SSR can cause localized segregation of constituent elements in the final product, generating structural defects during the synthesis.³⁶ Such structural defects would contribute directly to a decrease in photocatalytic activity, because they act as recombination centers for photogenerated electrons and holes, which has been demonstrated by transient absorption spectroscopy.^{37,38} On the other hand, such localized segregation of elements is not likely to occur in the PC method, as the constituent metals are atomically dispersed already in the precursor state. Thus, the less defective nature of the PC sample may lead to its higher activity.

2.1.2 Effects of Conduction Band Potentials and Number of Perovskite Layers: The cation composition of perovskite $\text{KCa}_2\text{Nb}_3\text{O}_{10}$ and its protonated form can be controllable, enabling us to study the effect of elemental compositions on photocatalytic activity. In metal oxides that contain transition metal cations of d^0 electronic configuration, the valence band is formed by O-2p orbitals, while the conduction band consists of empty d orbitals of transition metals coordinated by oxygen atoms.^{3,6} Thus, the B site cation has a strong impact on the formation of conduction band of perovskite oxide nanosheets. Although the A site cation does not directly contribute to the conduction band, it controls the distortion of O-B-O and B-O-B bonding angles, which also affects the conduction band edge potential (E_{CB}). The electronic band structure directly affects the light absorption properties, which also influence photocatalytic activity.

The composition of metal oxide nanosheets was optimized, aiming at maximizing their photocatalytic activity.³⁹ Dion-Jacobson type layered oxides of $\text{KCa}_{2-x}\text{Sr}_x\text{Nb}_{3-y}\text{Ta}_y\text{O}_{10}$ ($0 \leq x \leq 2$, $0 \leq y \leq 1.5$) were successfully synthesized by the PC method. Subsequent proton exchange and exfoliation with TBA^+OH^- resulted in $\text{Ca}_{2-x}\text{Sr}_x\text{Nb}_{3-y}\text{Ta}_y\text{O}_{10}^-$ nanosheets with lateral dimensions of approximately 500 nm, regardless of the compositional parameters x and y , as indicated by TEM observations. Structural analyses for the restacked $\text{HCa}_{2-x}\text{Sr}_x\text{-Nb}_{3-y}\text{Ta}_y\text{O}_{10}$ nanosheets by means of X-ray diffraction (XRD), Raman spectroscopy, and energy dispersive X-ray spectroscopy (EDS) confirmed the synthesis of a single-phase Dion-Jacobson perovskite with the target composition.

As expected, the substitution of A and B site cations in $\text{HCa}_2\text{Nb}_3\text{O}_{10}$ altered the light absorption properties of the material. Figure 6 shows UV-visible DRS for the restacked $\text{HCa}_{2-x}\text{Sr}_x\text{-Nb}_{3-y}\text{Ta}_y\text{O}_{10}$ nanosheets. The absorption edge shifted to longer wavelengths with increasing Sr content. The estimated band-gap energy decreased from 3.59 (for $x = 0$) to 3.40 eV (for $x = 2$). There are several factors that influence the band-gap energy of a layered perovskite consisting of NbO_6 octahedral units. For example, the distortion of NbO_6 units away from octahedral symmetry, the tilting of octahedra relative to each other, the thickness of the perovskite blocks, and the electronegativity of elements on the octahedral and 12-coordinate sites are major contributors.⁴⁰ In the present case, the distortion of NbO_6 units in the perovskite layers appears to be the main factor determining the band-gap energies. Because Sr^{2+} is located at the A site and has a larger ionic radius

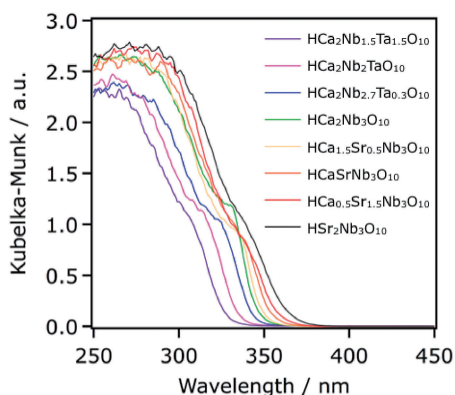


Figure 6. UV-visible DRS of restacked $\text{HCa}_{2-x}\text{Sr}_x\text{Nb}_3\text{O}_{10}$ and $\text{HCa}_2\text{Nb}_{3-y}\text{Ta}_y\text{O}_{10}$ nanosheets. Reproduced from Ref. 39 with permission. Copyright 2014 WILEY-VCH Verlag GmbH & Co. KGaA, Weinheim.

(1.58 Å) than Ca^{2+} (1.48 Å), the overlap of the Nb-4d orbital should be greater in the Sr-derivatives than in the Ca counterparts, relaxing the distortion of the NbO_6 octahedral units. The larger overlap of Nb-4d orbitals lowers the conduction-band energy (i.e., a positive shift in energy). On the other hand, increasing the Ta content led to a blue-shift of the absorption edge. The band gap energy is estimated from the absorption edge to be 3.80 eV for $y = 1.5$. The E_{CB} of Ta^{5+} -based oxides is located at more negative potentials than those of their Nb^{5+} analogues, because of the higher potential energy of Ta-5d orbitals relative to Nb-4d.^{3,6} The observed blue-shift should therefore originate from the negative shift of E_{CB} , which is supported by the recent work by Xu et al., who conducted electrochemical impedance spectroscopy for $\text{Ca}_{2-x}\text{Sr}_x\text{Nb}_{3-y}\text{Ta}_y\text{O}_{10}^-$ nanosheets to determine the flat-band potential (i.e., conduction band minimum).⁴¹ These results clearly demonstrate that perovskite nanosheets with controlled light absorption properties can be obtained by changing the composition. The E_{CB} values of the restacked $\text{HCa}_{2-x}\text{Sr}_x\text{Nb}_{3-y}\text{Ta}_y\text{O}_{10}$ nanosheets are summarized in Table 1.

Thus, the E_{CB} of three-layer perovskite nanosheet can be precisely tuned by altering its composition. Next, substitution effects of the A/B sites in $\text{Ca}_2\text{Nb}_3\text{O}_{10}^-$ nanosheets on H_2 evolution performance were examined. Table 1 also lists the apparent quantum yields (AQYs) of H_2 evolution on Pt-loaded nanosheet materials with different compositions. All of the tested samples showed very high AQYs, ranging from 40–80% at 300 nm. The AQY tends to decrease with increasing Sr content, presumably due to the positive shift of the conduction band edge that decreases the driving force of conduction-band electrons for driving proton reduction. On the other hand, increasing the Ta content in $\text{HCa}_2\text{Nb}_{3-y}\text{Ta}_y\text{O}_{10}$ increased the activity up to $y = 1$, beyond which it decreased slightly. The negative shift of E_{CB} in $\text{HCa}_2\text{Nb}_{3-y}\text{Ta}_y\text{O}_{10}$ with increasing Ta content is favorable for proton reduction to proceed. However, this gain is offset by inferior light-harvesting (Figure 6), which results in less efficient H_2 evolution. The best-performing material, $\text{HCa}_2\text{Nb}_2\text{TaO}_{10}$, produced H_2 without noticeable degradation, recording a maximum AQY of 80% at 300 nm. To the best of our knowledge, the approximately 80% AQY achieved by $\text{HCa}_2\text{Nb}_2\text{TaO}_{10}$ nanosheets is the highest among

Table 1. Estimated band gaps (E_g), conduction band potentials (E_{CB}) and photocatalytic activities of restacked $\text{HCa}_{2-x}\text{Sr}_x\text{Nb}_3\text{O}_{10}$ and $\text{HCa}_2\text{Nb}_{3-y}\text{Ta}_y\text{O}_{10}$ nanosheets

Nanosheets	E_g/eV	$E_{\text{CB}}^a/\text{V vs. Ag/AgNO}_3$	Apparent quantum yield at 300 nm ^b /%
$\text{HCa}_2\text{Nb}_3\text{O}_{10}$	3.59	-1.13	51 ± 4
$\text{HCa}_{1.5}\text{Sr}_{0.5}\text{Nb}_3\text{O}_{10}$	3.55	-1.11	48 ± 3
$\text{HCaSrNb}_3\text{O}_{10}$	3.50	-1.08	44 ± 5
$\text{HCa}_{0.5}\text{Sr}_{1.5}\text{Nb}_3\text{O}_{10}$	3.46	-1.06	39 ± 1
$\text{HSr}_2\text{Nb}_3\text{O}_{10}$	3.40	-1.03	39 ± 3
$\text{HCa}_2\text{Nb}_{2.7}\text{Ta}_{0.3}\text{O}_{10}$	3.65	-1.16	71 ± 5
$\text{HCa}_2\text{Nb}_2\text{TaO}_{10}$	3.76	-1.21	78 ± 2
$\text{HCa}_2\text{Nb}_{1.5}\text{Ta}_{1.5}\text{O}_{10}$	3.80	-1.23	65 ± 7

^aEstimated from the empirical correlation between the conduction band potential (E_{CB}) of metal oxide semiconductors containing d^0 and d^{10} metal ions and the band gaps (E_g): E_{CB} (V vs NHE) $\approx 1.23 - E_g/2$, which has been reported by Matsumoto (*J. Solid State Chem.* **1996**, *126*, 227). [Ag/AgNO_3] = [NHE] - 0.56. ^bReaction conditions: catalyst, 25 mg (0.5 wt % Pt-loaded); 10 vol. % aqueous methanol solution, 100 mL; light source, 300 W xenon lamp with a band-pass filter. Reproduced from Ref. 39 with permission. Copyright 2014 WILEY-VCH Verlag GmbH & Co. KGaA, Weinheim. Note that experimental E_{CB} values of d^0 metal oxide nanosheets obtained in the follow-up study by Xu et al. (ref 41) are consistent with the empirical values.

nanosheet-based photocatalysts reported so far, and even higher than the value recorded with the benchmark Pt/P25 TiO_2 photocatalyst (63%). The precise control of E_{CB} that maximizes the reactivity of the conduction-band electrons is responsible for the high photocatalytic activity of $\text{HCa}_2\text{Nb}_2\text{TaO}_{10}$. The 1.5 nm thickness and the high surface area of the perovskite oxide nanosheets are also both beneficial in terms of rapid migration of the photogenerated electrons and holes to the surface.

Another interesting comparison is the number of perovskite layers in metal oxide nanosheets. HLaNb_2O_7 is a Dion-Jacobson-type layered perovskite oxide that has double perovskite blocks. Although the conduction band minimum and other physicochemical properties of restacked HLaNb_2O_7 nanosheets are almost identical to those of $\text{HSr}_2\text{Nb}_3\text{O}_{10}$ (triple-perovskite), the photocatalytic H_2 evolution activity of the former is much lower than that of the latter, as shown in Figure 7.⁴² The considerable difference in activity between double- and triple-perovskites was also observed in layered $\text{RbLaTa}_2\text{O}_7$ (double-perovskite) and $\text{RbCa}_2\text{Ta}_3\text{O}_{10}$ (triple-perovskite), as reported by Machida et al.⁴³ Their theoretical studies suggested that the reactivity of holes in the O-2p valence band with intercalated molecules varied with respect to the number of perovskite layers, and that the terminal oxygen atoms facing the interlayer galleries in the triple perovskite made a strong contribution to the formation of the valence band maximum, whereas those in the double perovskite did not. As a result, the triple perovskite exhibited a higher reactivity than the double-layer analog.

2.1.3 Effect of Interlayer Cations: Interlayer cations in the perovskite nanosheets are another compositional parameter that can affect the physicochemical properties of the restacked

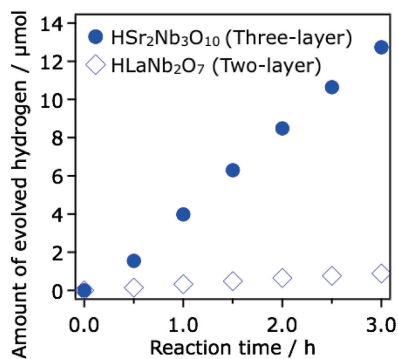


Figure 7. Time courses of H₂ evolution from Pt-loaded restacked nanosheets of HSR₂Nb₃O₁₀ and HLaNb₂O₇ under UV irradiation ($\lambda > 300$ nm). Reaction conditions: catalyst, 5.0 mg; 1 M aqueous 2-propanol solution, 2.0 mL; light source, 300 W xenon lamp. Reproduced from Ref. 42 with permission from The Royal Society of Chemistry.

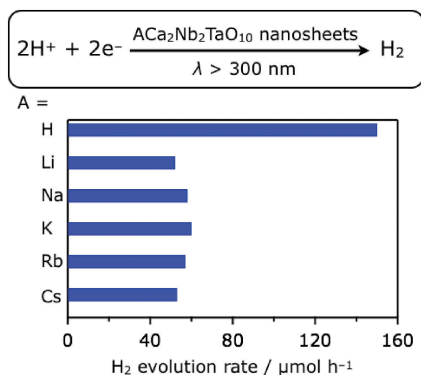


Figure 8. Photocatalytic activities of Ca₂Nb₂TaO₁₀⁻ nanosheets restacked by various agents for H₂ evolution under UV irradiation ($\lambda > 300$ nm). Reaction conditions: catalyst, 100 mg (0.5 wt % Pt-loaded in-situ); 10 vol. % aqueous methanol solution, 100 mL; light source, 300 W xenon lamp. Reproduced from Ref. 44 with permission from The Royal Society of Chemistry.

form of the nanosheets. It was possible to change the interlayer cations of restacked Ca₂Nb₂TaO₁₀⁻ nanosheets by simply applying various acids, bases, and salts that contain different cations.⁴⁴ This method produced restacked nanosheet materials having different morphological features and different degrees of interlayer hydration. However, the interlayer cations had little effect on the light absorption properties of the restacked Ca₂Nb₂TaO₁₀⁻ nanosheets. This is as expected because photoexcitation from the valence band that consists of O-2p orbitals to the conduction band formed by the empty Nb-4d and Ta-5d orbitals occurs in the two-dimensional nanosheet, independent of the interlayer cation.

The restacked Ca₂Nb₂TaO₁₀⁻ nanosheets with various interlayer cations were tested as photocatalysts for H₂ evolution from aqueous methanol solution. The highest activity was obtained for the one restacked with HCl, as shown in Figure 8. Results of structural analyses and photocatalytic reactions suggested that the high activity resulted from interlayer protonation, which is favorable for the oxidation reaction.

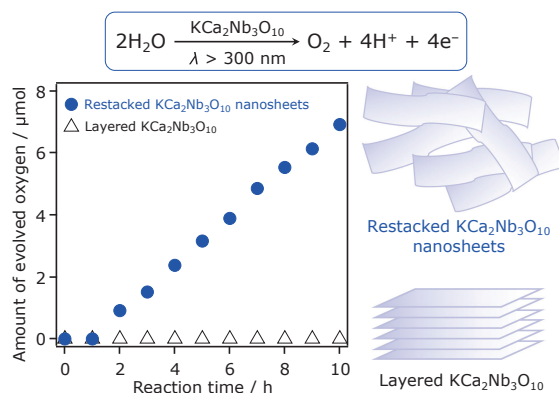


Figure 9. Time courses of water oxidation to O₂ using KCa₂Nb₃O₁₀-based materials under UV irradiation ($\lambda > 300$ nm). Reaction conditions: catalyst, 50 mg; 10 mM aqueous NaIO₃ solution, 100 mL; light source, 300 W xenon lamp. Reproduced from Ref. 45.

2.2 Oxygen Evolution Activity. 2.2.1 Exfoliation-Induced Water Oxidation Activity:

Metal oxide semiconductors are generally good photocatalysts for water oxidation due to the very positive valence band potential, which results in a large driving force for water oxidation.^{3,6} Early studies focusing on water oxidation over metal oxides such as rutile TiO₂ have shown that high crystallinity of the semiconductor is prerequisite for efficient water oxidation.¹⁰ In this regard, metal oxide nanosheets are advantageous as water oxidation photocatalysts because of their single-crystalline texture and high surface area.

Photocatalytic water oxidation to produce O₂ was first performed using restacked KCa₂Nb₃O₁₀ nanosheets in the presence of IO₃⁻ as a reversible electron acceptor.⁴⁵ The Gibbs free energy change of the overall reaction is positive, making this a so-called nonsacrificial, artificial photosynthetic type reaction. While layered KCa₂Nb₃O₁₀ exhibited no activity, O₂ evolution was clearly observable using restacked KCa₂Nb₃O₁₀ nanosheets under the same reaction conditions (Figure 9). Ion-chromatography analysis indicated that the amount of I⁻ in the liquid phase, which was produced as a result of reduction of IO₃⁻, corresponded to two thirds of the O₂ production, consistent with the amount expected from the stoichiometry. No reaction took place without NaIO₃.

The induced activity of water oxidation may seem to result from an enlarged surface area of restacked nanosheets, but could not be explained simply by the specific activity (vs. surface area). This suggests that the exfoliation and restacking process itself is important for inducing the nonsacrificial water photooxidation activity of KCa₂Nb₃O₁₀. The exfoliation-restacking process produces disordered nanosheet aggregates as described earlier (see Figure 3), which may be advantageous for incorporating the reactant molecules (i.e., water) inside the nanospace formed between nanosheets, leading to high activity. The importance of intercalation of H₂O into the interlayer galleries to improve photocatalytic water oxidation activity was demonstrated using a Ruddlesden–Popper phase layered perovskite, K₂CaNaNb₃O₁₀.⁴⁶ Because the absorption edge of restacked KCa₂Nb₃O₁₀ was blue-shifted relative to the layered one due to quantum size effects caused by the nanosized

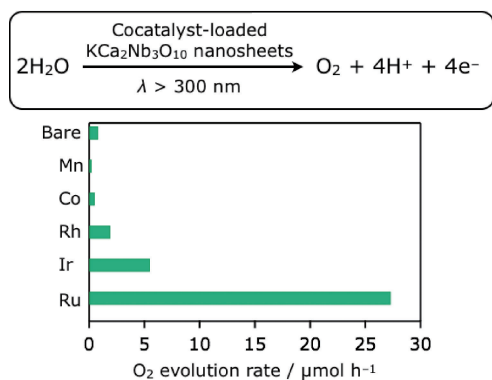


Figure 10. O₂ evolution rate over various metal oxides (0.1 wt %) loaded onto restacked KCa₂Nb₃O₁₀ under UV irradiation ($\lambda > 300$ nm). Reaction conditions: catalyst: 50 mg; 10 mM aqueous NaIO₃ solution, 100 mL; light source, 300 W xenon lamp. Reproduced from Ref. 47 with permission. Copyright 2016 WILEY-VCH Verlag GmbH & Co. KGaA, Weinheim.

thickness of the nanosheet, the resulting larger band gap of the restacked nanosheets may be another factor that positively affected the water oxidation activity.

2.2.2 Effect of Cocatalyst Loading: Because the non-sacrificial oxidation of water using IO₃⁻ as an electron acceptor involves the 6-electron reduction of IO₃⁻ and 4-electron oxidation of water, it is expected that introduction of a suitable cocatalyst onto the semiconductor photocatalyst will improve the activity. For restacked KCa₂Nb₃O₁₀ nanosheets, loading 0.1 wt % ruthenium oxide (RuO_x) dramatically promoted the O₂ evolution rate, with an AQY of $3.6 \pm 0.1\%$ at 300 nm.⁴⁵ Although RuO_x loading was also effective for enhancing water oxidation by layered KCa₂Nb₃O₁₀, the promotional effect was much greater for restacked KCa₂Nb₃O₁₀ than for the bulk layered photocatalyst. This result further supports the idea that the exfoliation–restacking process is essential to inducing the water oxidation activity of KCa₂Nb₃O₁₀.

Not only RuO_x but also other metal oxides were tested as promoters for the water oxidation reaction.⁴⁷ Oxides of rhodium and iridium gave higher O₂ evolution rates, compared to unloaded materials. Among the metal oxides tested, RuO_x yielded the highest activity (Figure 10). On the other hand, a well-known metal oxide cocatalyst for water oxidation, CoO_x, decreased the activity. Previous studies have shown that ruthenium oxide promoted the reduction of IO₃⁻,⁴⁸ and that iridium and rhodium oxides could serve as reduction sites for protons.^{6,9} Thus, one can conclude that the O₂ evolution activity of restacked KCa₂Nb₃O₁₀ nanosheets is enhanced when a reduction cocatalyst is deposited. As mentioned earlier, the reduction of IO₃⁻ involves a 6-electron process that could be a kinetic bottleneck in the absence of a catalyst. Abe et al. have reported that the overpotentials for electrochemical reduction of IO₃⁻ on rhodium oxide and iridium oxide are lower than that observed using cobalt oxide, and ruthenium oxide showed the lowest overpotential.⁴⁹ These results indicate that the reduction of IO₃⁻ is the rate-determining step in the water oxidation reaction. Acceleration of the reduction of IO₃⁻ should therefore lead to enhanced water oxidation activity.

2.2.3 Effect of Physicochemical Properties: Physicochemical properties of nanosheets (e.g. size, composition, and so on) were shown to have a strong influence on the photocatalytic H₂ evolution activity, as discussed earlier. Next, structural effects of KCa_{2-x}Sr_xNb₃O₁₀ nanosheets on O₂ evolution were investigated with the aid of the RuO_x cocatalyst. In contrast to H₂ evolution that was influenced by the lateral size of nanosheets [i.e., the second calcination temperature in the PC synthesis (here 1123–1423 K) of the host KCa₂Nb₃O₁₀], no noticeable correlation between the lateral size (as well as specific surface area) and O₂ evolution activity of restacked KCa₂Nb₃O₁₀ nanosheets was observed.⁴⁷ The O₂ evolution activity was also insensitive to the preparation method; both PC and SSR methods gave almost the same activity. These results indicate that structural properties of the nanosheets (such as crystallinity and defect density) have little impact on the photocatalytic activity for water oxidation to form O₂. One plausible explanation for the structure-insensitive activity of restacked KCa₂Nb₃O₁₀ nanosheets is that the reduction of IO₃⁻ is still simply the rate-determining step in the reaction, as discussed above.

On the other hand, the O₂ evolution activity increased moderately with increasing Sr concentration in restacked KCa_{2-x}Sr_xNb₃O₁₀ nanosheets having identical surface area ($\sim 30 \text{ m}^2 \text{ g}^{-1}$). Here the E_{CB} potentials of the restacked KCa_{2-x}Sr_xNb₃O₁₀ nanosheets are positively shifted with an increase in the Sr content, as discussed earlier. This positive shift of E_{CB} is disadvantageous with regard to the reduction of IO₃⁻ (+1.08 V vs. NHE at pH = 0) in terms of the driving force for the reaction. However, the trend observed in the photocatalytic activities was opposite. Because the driving force for IO₃⁻ reduction is sufficiently large compared to the differences in the conduction band energies of these materials (0.1–0.3 V), the differences in E_{CB} appear to have little impact on the activity for water oxidation. Another possible factor affecting activity is the light absorption properties of the restacked nanosheets. That is, the KSr₂Nb₃O₁₀ nanosheets that possess the smallest band gap among the tested materials are able to absorb the incident photon flux more efficiently and thus to generate a greater number of photoexcited charge carriers. The more efficient utilization of incident photons will lead to an increase in the number of photogenerated charge carriers, which might facilitate electron transfer from the nanosheets to the RuO_x, resulting in higher activity.

2.3 Overall Water Splitting. **2.3.1 A New Interlayer Modification Method:** Metal oxide nanosheets are thus good photocatalysts for the individual H₂ and O₂ evolution reactions. However, there are only a few reports of overall water splitting using nanosheet photocatalysts, in contrast to bulk type oxide systems where more than 100 materials have been reported to show overall water splitting activity.³ It has been suggested by several researchers that certain metal oxide nanosheets could utilize their interlayer as reaction sites.^{20,21,23,50,51} Study by Ebina et al. using restacked Ca₂Nb₃O₁₀⁻ nanosheets claimed that modification of the interlayer nanospace of the restacked material with a RuO_x cocatalyst was essential to achieving overall water splitting.²¹ Therefore, effective modification of the interlayer space with a suitable cocatalyst appears to be the key to achieve the reaction. Besides Ebina's work, Mallouk,

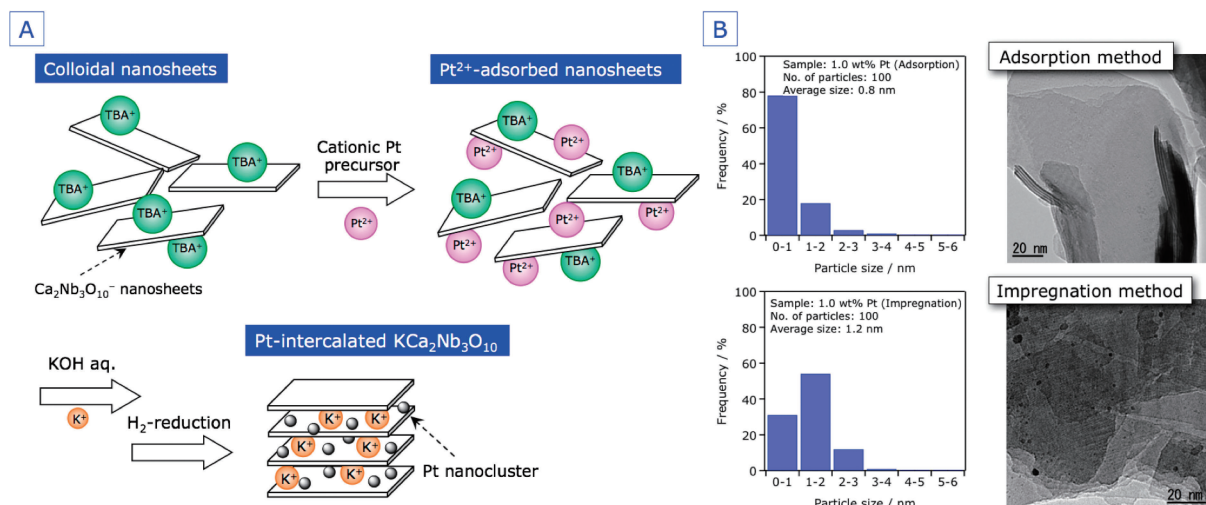


Figure 11. (A) Schematic illustration of the preparation of Pt-intercalated $\text{KCa}_2\text{Nb}_3\text{O}_{10}$ nanosheets through electrostatic attraction between a cationic complex and anionic nanosheets [TBA⁺ indicates tetra(*n*-butyl)ammonium cation]. (B) Typical TEM images and corresponding particle size distributions of restacked $\text{KCa}_2\text{Nb}_3\text{O}_{10}$ nanosheets modified with 1.0 wt% Pt using an adsorption and impregnation method. Reproduced from Ref. 53 with permission. Copyright 2015 WILEY-VCH Verlag GmbH & Co. KGaA, Weinheim.

et al. have reported the incorporation of $\text{Rh}(\text{OH})_3$ or Rh_2O_3 nanoparticle cocatalysts in the interlayer nanospace of restacked nanosheets (or nanoscrolls).^{23,52} While the thus-developed Rh_2O_3 -intercalated $\text{HCa}_2\text{Nb}_3\text{O}_{10}$ nanosheets exhibited excellent performance for H_2 evolution from aqueous methanol, an appropriate method of interlayer modification to achieve overall water splitting had not been developed until recently.

A new interlayer modification method, which utilizes electrostatic interaction between the negatively charged $\text{Ca}_2\text{-Nb}_3\text{O}_{10}^-$ nanosheets and a cationic precursor of the cocatalyst, was developed.⁵³ Figure 11A illustrates the preparation procedure. First, an aqueous solution containing a dissolved cationic Pt complex (e.g., $[\text{Pt}(\text{NH}_3)_4]\text{Cl}_2 \cdot \text{H}_2\text{O}$) was added to the TBA⁺-stabilized $\text{Ca}_2\text{Nb}_3\text{O}_{10}^-$ nanosheet suspension, followed by stirring for 24 h to allow the metal precursor ions to adsorb onto the surface of the nanosheets. Then, KOH was added to precipitate the colloidal nanosheets, followed by drying in an oven overnight and heating under a H_2 stream to reduce the cationic Pt species. In this Account, this method is referred to as the adsorption method.

Physicochemical analyses for the as-prepared material showed that Pt nanoclusters smaller than 1 nm in size were intercalated into the interlayer nanospace of restacked $\text{KCa}_2\text{Nb}_3\text{O}_{10}$ nanosheets (Figure 11B), although there were some Pt nanoparticles deposited on the external surface of the material. On the other hand, the interlayer modification of Pt was unsuccessful when an anionic Pt precursor such as $\text{H}_2[\text{PtCl}_6] \cdot 6\text{H}_2\text{O}$ was used. These results indicate that electrostatic interaction plays an essential role during the adsorption method in depositing Pt inside the restacked $\text{KCa}_2\text{Nb}_3\text{O}_{10}$ nanosheets. For comparison, Pt was loaded on the restacked $\text{KCa}_2\text{Nb}_3\text{O}_{10}$ nanosheets by an impregnation method using $[\text{Pt}(\text{NH}_3)_4]\text{Cl}_2 \cdot \text{H}_2\text{O}$ as a precursor, followed by thermal H_2 reduction under the same conditions. In this case, Pt was deposited exclusively on the external surface, not in the interlayers, with an average

particle size of 1.8 nm (Figure 11B), which is obviously larger than that obtained by the adsorption method. The successful deposition of smaller Pt particles by the adsorption method is likely to originate from steric hindrance of the interlayer nanospace, in which the Pt species sandwiched by $\text{Ca}_2\text{Nb}_3\text{O}_{10}^-$ nanosheets in the adsorption samples is less susceptible to aggregation upon thermal treatment. It is also noted that the intercalated Pt nanoclusters strongly interact with the nanosheet surface, as indicated by X-ray photoelectron spectroscopy, similar to the Rh_2O_3 -intercalated $\text{HCa}_2\text{Nb}_3\text{O}_{10}$ nanosheet system.²³ This is favorable for the charge transfer process between the semiconductor photocatalyst and cocatalyst, as the efficiency of photocatalytic reactions can be improved with intimate contact between the semiconductor and the cocatalyst. This adsorption method utilizing simple electrostatic interactions between the anionic nanosheets and cationic precursors is applicable to various metal species. For example, intercalation of highly dispersed Pd, Rh and Ru into the interlayer galleries of restacked $\text{KCa}_2\text{Nb}_3\text{O}_{10}$ nanosheets was possible to effect in a similar manner.

The overall water splitting reaction was performed using the as-prepared $\text{Pt}/\text{KCa}_2\text{Nb}_3\text{O}_{10}$ nanosheets under UV irradiation ($\lambda > 300 \text{ nm}$). To minimize the negative impact of H_2/O_2 recombination that occurs on Pt, a small amount of NaI was added to the reactant solution.⁵⁴ While unmodified restacked $\text{KCa}_2\text{Nb}_3\text{O}_{10}$ nanosheets produced only a small amount of H_2 , $\text{Pt}/\text{KCa}_2\text{Nb}_3\text{O}_{10}$ restacked nanosheets prepared by both adsorption and impregnation methods produced H_2 and O_2 simultaneously. The rates of H_2 and O_2 evolution by the adsorption sample were faster than those of the impregnation sample (Figure 12), most likely because of the smaller size of the Pt deposits. The activity of the adsorption sample was substantially higher than that of the RuO_x -deposited one, which was prepared according to the method of Ebina et al.²¹ To our knowledge, the water splitting activity of the adsorption sample is the highest among nanosheet-based photocatalysts ever

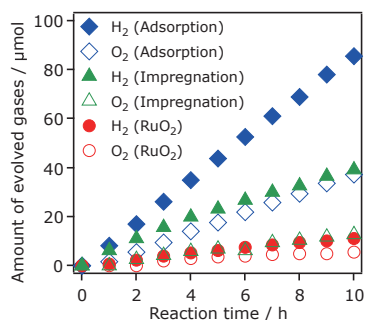


Figure 12. Time courses of overall water splitting using $\text{KCa}_2\text{Nb}_3\text{O}_{10}$ -based materials under UV irradiation ($\lambda > 300 \text{ nm}$). Reaction conditions: catalyst, 50 mg; 10 mM aqueous NaI solution, 100 mL; light source, 300 W xenon lamp. Reproduced from Ref. 53 with permission. Copyright 2015 WILEY-VCH Verlag GmbH & Co. KGaA, Weinheim.

reported. In addition to the higher performance, the Pt-intercalated $\text{KCa}_2\text{Nb}_3\text{O}_{10}$ nanosheets were stable over 30 h of reaction, producing H_2 and O_2 continuously. The total amount of H_2 and O_2 evolved in 30 h of reaction (573 μmol) was much greater than that of the Pt/ $\text{KCa}_2\text{Nb}_3\text{O}_{10}$ used (ca. 90 μmol), providing confirmation of the catalytic cycle of the reaction. The AQY of overall water splitting was estimated to be about 3% at 300 nm.

So far, the size effect of the cocatalyst on the photocatalytic water splitting performance has been investigated, with the use of precisely controlled metal nanoparticles.^{55–57} However, there are very few reports or such effects with sizes smaller than 1 nm because of the lack of an effective preparation method and a suitable photocatalyst. Therefore, the results of this work demonstrated the superior ability of metal nanoclusters with sizes smaller than 1 nm to promote photocatalytic water splitting reaction for the first time.

2.3.2 Effect of Physicochemical Characteristics of Pt/ $\text{KCa}_2\text{Nb}_3\text{O}_{10}$ Nanosheets on Activity: The Pt/ $\text{KCa}_2\text{Nb}_3\text{O}_{10}$ system was further studied as a photocatalyst for overall water splitting, with respect to the physicochemical properties of the deposited Pt.⁵⁸ In the adsorption method (Figure 11A), the Pt precursor cation incorporated into the restacked $\text{KCa}_2\text{Nb}_3\text{O}_{10}$ nanosheets is subject to thermal H_2 treatment. In general, the H_2 -reduction temperature influences the physicochemical properties of the deposited metal, resulting in different properties as cocatalysts.

Deposition of Pt on restacked $\text{KCa}_2\text{Nb}_3\text{O}_{10}$ nanosheets was performed at different H_2 -reduction temperatures. At temperatures below 673 K, Pt nanoparticles smaller than 2 nm were observed, although the size distribution was somewhat different at each temperature. In particular, most of the Pt deposits were smaller than 1 nm when reduced at 473 K. Increasing the reduction temperature led to exclusion of the intercalated Pt nanoparticles from the interlayer nanospace to the external surface of the restacked $\text{KCa}_2\text{Nb}_3\text{O}_{10}$ nanosheets, due to the reconstruction of the original layered structure of $\text{KCa}_2\text{Nb}_3\text{O}_{10}$, as revealed by XRD analysis. This also changed the oxidation state of the Pt species from the oxide to the metal, which is reasonable considering their greater exposure to the reducing

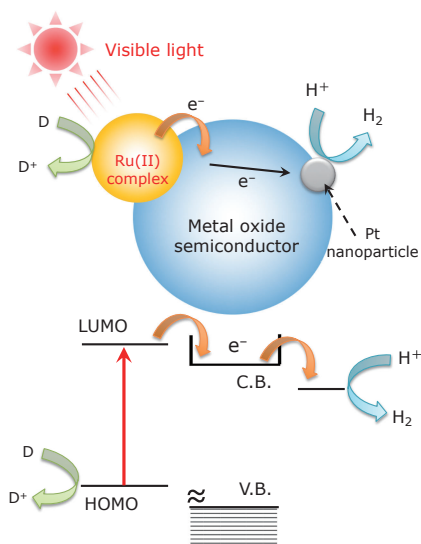


Figure 13. Schematic illustration of H_2 evolution from water using a wide-gap oxide semiconductor and a Ru(II) complex photosensitizer under visible light.

atmosphere at high temperatures. The activity of Pt/ $\text{KCa}_2\text{Nb}_3\text{O}_{10}$ restacked nanosheets for overall water splitting was dependent on the feature size and the oxidation state of Pt. More importantly, the intercalated, electron-deficient Pt species realized at 473 K were advantageous in terms of suppressing undesirable backward reactions such as reduction of O_2 and/or H_2/O_2 recombination. High temperature reduction was undesirable, because it caused generation of aggregated Pt^0 species, which worked poorly as promoters on the external surface of restacked $\text{KCa}_2\text{Nb}_3\text{O}_{10}$ nanosheets.

3. Dye-Sensitized H_2 Evolution under Visible Light

3.1 Activation of Wide-Gap Metal Oxides toward Visible-Light Photocatalysis. For efficient solar energy conversion, it is necessary to utilize visible light, which occupies approximately half of the solar spectrum. As described above, metal oxide nanosheets work as good photocatalysts for H_2/O_2 half reactions and overall water splitting. However, they work only under UV irradiation ($< 400 \text{ nm}$) because their band gaps are too wide to absorb visible light. The wide band gap of metal oxides originates from their band structure, where the valence band maximum is formed by O-2p orbitals. The position of the O-2p orbitals in metal oxides with d^0 - or d^{10} -electronic configurations is located at ca. +3 V.⁵⁹ Therefore, if a metal oxide satisfies the thermodynamic potential for overall water splitting, the band gap of the oxide should inevitably exceed 3 eV, which limits the utilization of visible light.

One of the strategies for activating a wide-gap metal oxide toward visible-light photocatalysis is to modify it with a redox photosensitizer (or dye molecules) that can absorb visible light.^{60–62} Figure 13 illustrates the basic principle of a sensitized metal oxide for H_2 evolution, which is essentially the same as in dye-sensitized solar cells.⁶³ Upon photoexcitation of a redox photosensitizer adsorbed on the metal oxide surface, electron injection occurs from the excited state of the sensitizer to the conduction band of the oxide (i.e., oxidative quenching of the sensitizer), producing the one-electron oxidized state

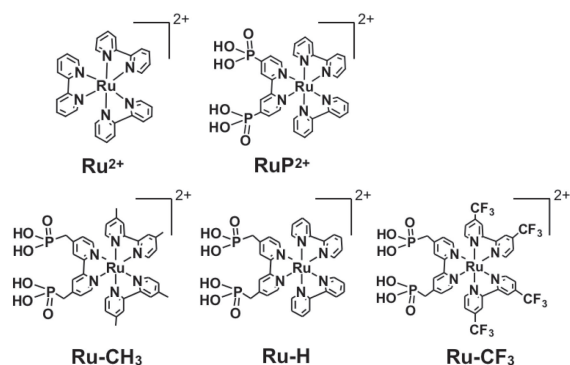


Figure 14. Ru(II)-based photosensitizers.

of the sensitizer. The injected electron in the metal oxide is consumed at a catalytic site such as Pt, while the oxidized sensitizer is regenerated by accepting an electron supplied from a suitable electron donor. Here the ultimate electron donor is water, but to avoid the complication of water oxidation catalysis, a strong electron donor such as ethylenediaminetetraacetic acid (EDTA) or triethanolamine (TEOA) is usually used.

3.2 Metal Oxide Nanosheets as Building Blocks for Sensitized H₂ Evolution. The primary requirement to realize efficient dye-sensitized H₂ evolution is to bind photosensitizer molecules to the metal oxide surface, because the excited-state lifetime of a photosensitizer is typically too short to allow for diffusion of the molecule to the oxide surface.⁶¹ Ruthenium(II) trisdiimine [Ru(bpy)₃²⁺, bpy = 2,2'-bipyridine; abbreviated as Ru²⁺, see Figure 14] and its derivatives are representative redox photosensitizers for dye-sensitized H₂ evolution.^{61,62} For efficient electron injection, photosensitizers need to be anchored to the metal oxide surface. In the case of Ru(II) trisdiimine complexes, the diimine ligands are typically functionalized with carboxylic acid or phosphonic acid groups.⁶² While such chemical modification of redox photosensitizers is usually necessary, one may expect that unmodified, cationic Ru²⁺ is immobilized on the metal oxide nanosheets through electrostatic attraction even without functionalization of the bpy ligand, because the surface of metal oxide nanosheets is intrinsically negatively-charged. It is also noted that the single-crystalline texture of nanosheets and their high surface area may be advantageous over bulk-type oxide semiconductors such as TiO₂.

On the basis of these ideas, scrolled niobate nanosheets (Nb₆O₁₇⁴⁻), which can be readily prepared by exfoliation of proton-exchanged lamellar K₄Nb₆O₁₇ with TBA⁺OH⁻, were investigated as the building block for sensitized H₂ evolution.⁶⁴ The Nb₆O₁₇⁴⁻ sheets do not possess mirror symmetry, meaning that the individual sheet is asymmetric. Therefore, there is an intrinsic tension in the sheet, which leads to spontaneous scrolling in order to release the strain energy.⁶⁵ The exfoliated, scrolled Nb₆O₁₇⁴⁻ sheets were reassembled by reaction with HCl. TEM images of the as-prepared material, represented as NS-H₄Nb₆O₁₇ (NS = nanoscroll), are shown in Figure 15A. The diameters of NS-H₄Nb₆O₁₇ are approximately 30 nm, with lengths of several hundred nanometers. The specific surface area of NS-H₄Nb₆O₁₇ was 250–300 m² g⁻¹, much larger than that of the proton-exchanged parent solid prior to exfoliation

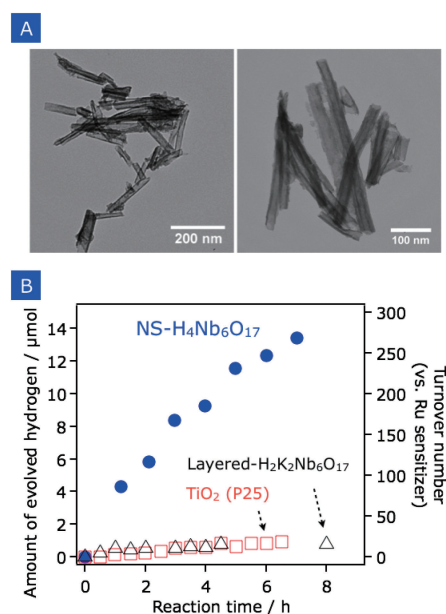


Figure 15. (A) TEM images of the as-prepared NS-K₄-Nb₆O₁₇. (B) Time courses of H₂ evolution from 0.1 wt % Pt-loaded semiconductors sensitized by Ru²⁺ with visible light ($\lambda > 420$ nm). Reaction conditions: catalyst, 5.0 mg; aqueous solution containing 10 mM EDTA and 50 μ M Ru²⁺, 2.0 mL; light source, 300 W xenon lamp with a cutoff filter. Reproduced from Ref. 64 with permission. Copyright 2008 American Chemical Society.

(ca. 1–2 m² g⁻¹). Importantly, zeta-potential measurements indicated that the surface of NS-H₄Nb₆O₁₇ is negatively charged in the pH range of 3–11.

NS-H₄Nb₆O₁₇ modified with Pt nanoparticles was then used as a building block for dye-sensitized H₂ evolution under visible light using Ru²⁺ in the presence of EDTA as a sacrificial electron donor. For comparison, layered K₄Nb₆O₁₇ and P25 TiO₂ were also tested. Adsorption experiments indicated that the negatively-charged NS-H₄Nb₆O₁₇ bound cationic Ru²⁺ from the reactant solution almost quantitatively (here 20 μ mol g⁻¹) under the reaction conditions (pH 5.5), while only 10–20% of Ru²⁺ in the solution was adsorbed onto layered K₄Nb₆O₁₇ and P25 TiO₂. XRD measurements also showed that Ru²⁺ was almost exclusively adsorbed on the external surface of NS-H₄Nb₆O₁₇. As shown in Figure 15B, the H₂ evolution activity of the nanoscroll-based system was an order of magnitude higher than those of similarly sensitized P25 titania and the parent layered material. This significant difference in activity is due primarily to the superior ability of the nanoscroll to bind Ru²⁺, as mentioned earlier, which allows for electron injection from the excited-state of the sensitizer and subsequent H₂ evolution. Importantly, NS-H₄Nb₆O₁₇ gave much higher activity for sensitized H₂ evolution than the parent layered material, even though the same amount of Ru²⁺ was adsorbed, clearly indicating superior functionality of niobate nanoscrolls as the building block for dye-sensitized H₂ evolution. The AQY for the nanoscroll-based system was approximately 5% at 450 \pm 20 nm.⁶⁶ The turnover number (TON) for H₂ evolution, which was calculated based on the molar amount of Ru²⁺ employed, far exceeded 1, indicating that the reaction

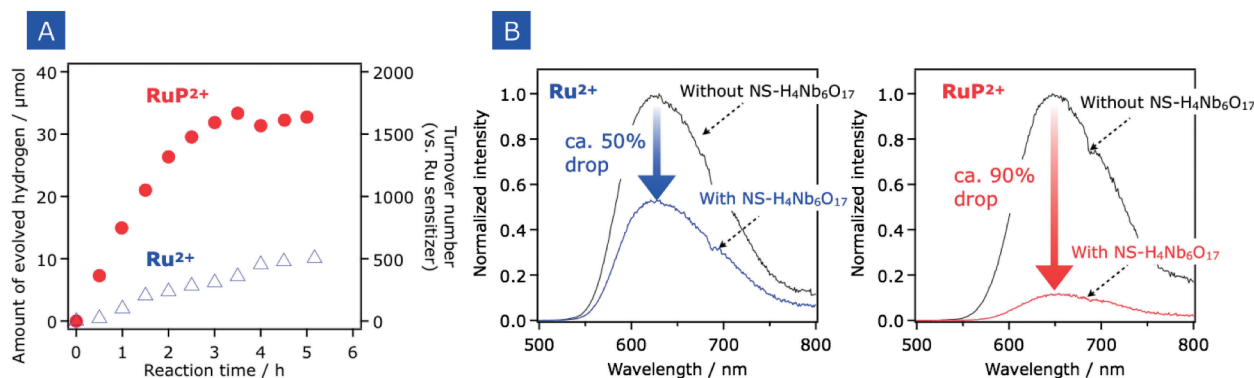


Figure 16. (A) Time courses of H₂ evolution from 0.3 wt % Pt-loaded NS-H₄Nb₆O₁₇ sensitized by **RuP²⁺** or **Ru²⁺** (8.0 μmol g⁻¹) with visible light ($\lambda > 420$ nm). Reaction conditions: catalyst, 5.0 mg; 0.01 M aqueous EDTA solution, 2.0 mL; light source, 300 W xenon lamp with a cutoff filter. (B) Steady-state emission spectra for 0.3 wt % Pt-loaded NS-H₄Nb₆O₁₇ sensitized by **RuP²⁺** or **Ru²⁺** with 450 nm excitation. The spectra were acquired at room temperature under Ar atmosphere using aqueous EDTA solution (0.01 M, 2.0 mL) containing 0.3 wt % Pt-loaded NS-H₄Nb₆O₁₇ (5.0 mg) adsorbed with **RuP²⁺** or **Ru²⁺** (8.0 μmol g⁻¹). Reproduced from Ref. 67 with permission. Copyright 2009 American Chemical Society.

was catalytically cycled. A follow-up study also found that restacked HCa₂Nb₃O₁₀ nanosheets achieved a similar functionality for dye-sensitized H₂ evolution.⁴²

3.3 Comparison of H₂ Evolution Activity: Electrostatic vs. Chemical Anchoring. Thus, even without any chemical bond linkage between the sensitizer and the nanoscroll surface, an efficient sensitized H₂ evolution system could be constructed through the use of negatively-charged metal oxide nanoscrolls (or nanosheets). Nevertheless, it is intriguing to compare electrostatic vs. traditional chemical anchoring in the nanosheet-based dye-sensitized H₂ evolution system. Bae and Choi have examined the effects of anchoring groups on sensitized H₂ evolution using Ru(II) trisdiimine complexes and Pt/TiO₂. Among the Ru(II)-based sensitizers they examined, Ru(bpy)₂-(4,4'-(PO₃H₂)₂bpy)²⁺ (abbreviated as **RuP²⁺**, Figure 14) was found to be the most effective.⁶² The strong binding of **RuP²⁺** with the metal oxide surface would address the competition of EDTA and **Ru²⁺** for adsorption sites on the nanoscroll surface, which limits the AQY and TON.

Thus, H₂ evolution activities of Pt/NS-H₄Nb₆O₁₇ sensitized by **Ru²⁺** and **RuP²⁺** were compared.⁶⁷ As shown in Figure 16A, **RuP²⁺** functioned more efficiently than **Ru²⁺**, giving an AQY of ca. 25% at 450 ± 20 nm and a TON of greater than 1500, which were roughly 3 times greater than those obtained with **Ru²⁺**.

Ru(II) trisdiimine type complexes exhibit emission as a result of ¹MLCT photoexcitation, and the excited state is quenched in the presence of semiconductor particles if electron transfer from one side to the other occurs.^{68,69} Here the excited state oxidation potentials of **Ru²⁺** and **RuP²⁺** are both negative enough to inject electrons into the conduction band of NS-H₄Nb₆O₁₇. Steady-state emission spectroscopy was thus employed to investigate the oxidative quenching of the ³MLCT excited-state by NS-H₄Nb₆O₁₇ for **Ru²⁺** and **RuP²⁺** under the same conditions as photocatalytic reactions. In both cases, the emission intensity of the sensitizer decreased upon addition of NS-H₄Nb₆O₁₇ to the aqueous solution containing the sensitizer, as shown in Figure 16B. The observed drop in emission intensity arises from the oxidative quenching of the excited state

sensitizer via electron injection into NS-H₄Nb₆O₁₇. Importantly, the efficiency of quenching was greater for **RuP²⁺** (ca. 90%) than for **Ru²⁺** (ca. 50%), suggesting stronger electronic coupling between **RuP²⁺** and NS-H₄Nb₆O₁₇ than with electrostatically bound **Ru²⁺**. The greater quenching efficiency observed in the **RuP²⁺**-based system could thus account for its substantially faster H₂ evolution rate.

3.4 Effect of Excited-State Oxidation Potential of Ru(II) Photosensitizers. The HOMO/LUMO potentials of metal complex photosensitizers can be tuned by appropriate design of the complex. For example, the LUMO potential (as well as excited state oxidation potential, E_{ox}^*) of Ru(II) trisdiimine complexes can be controlled by introduction of an electron withdrawing or donating moiety into the diimine ligand.⁷⁰ This enables us to investigate the effect of the excited state oxidation potential on the efficiency of sensitized H₂ evolution. Thus, Ru(II) photosensitizers with different LUMO potentials, **Ru-CH₃**, **Ru-H**, and **Ru-CF₃** (see Figure 14), were applied to the H₂ evolution system using restacked HCa₂Nb₃O₁₀ nanosheets modified with Pt nanoparticles.⁷¹ Figure 17A shows that **Ru-CH₃** or **Ru-H** served as effective photosensitizers with Pt/HCa₂Nb₃O₁₀ nanosheets to produce H₂ catalytically with visible light excitation, while **Ru-CF₃** did not.

As demonstrated earlier, electron injection efficiency from the excited state of the photosensitizer to the conduction band of semiconductor has a strong influence on sensitized H₂ evolution. Here the relative electron injection efficiencies from the excited state of a Ru(II) photosensitizer to the niobate nanosheet were investigated using porous electrodes of Ca₂Nb₃O₁₀⁻ nanosheet aggregates modified with a Ru(II) photosensitizer as photoanodes. Because the Ca₂Nb₃O₁₀⁻ nanosheet is an n-type semiconductor, it serves as a photoanode material,⁷² and it is possible to monitor the electron injection event by observing photocurrent flowing in the cell. In this case, only the adsorbed Ru(II) photosensitizers undergo photoexcitation with visible light, while the niobate nanosheet does not due to its large band gap. The result of photoelectrochemical measurements, which were conducted under intermittent visible light ($\lambda > 420$ nm) in an aqueous Na₂SO₄ solution (0.1 M) containing 10 mM EDTA,

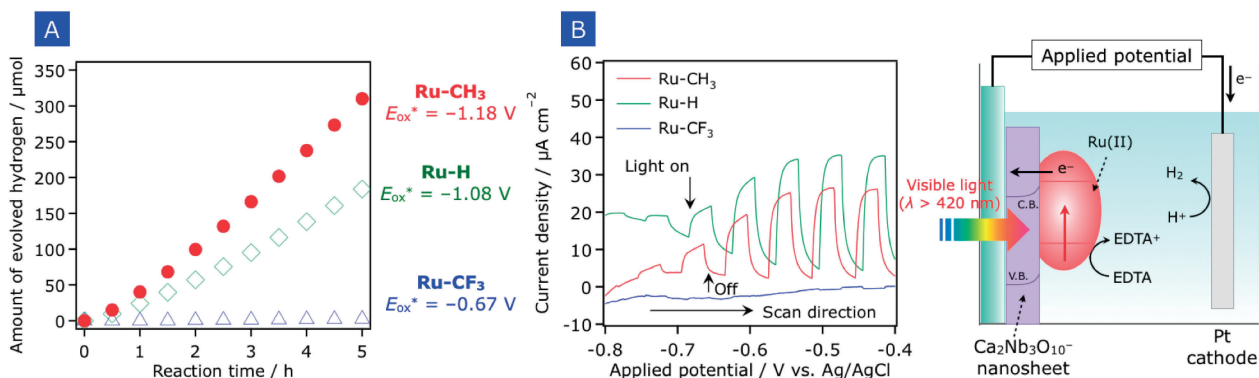


Figure 17. (A) Time courses of H₂ evolution on 0.5 wt% Pt-loaded HCa₂Nb₃O₁₀ nanosheets sensitized by different Ru(II) complexes (8.0 μmol g⁻¹) under visible light (λ = 420 nm). Reaction conditions: catalyst, 25 mg; 10 mM aqueous EDTA solution, 100 mL; light source, 300 W xenon lamp with a band-pass filter. (B) Current–voltage curves for KCa₂Nb₃O₁₀ nanosheet electrodes sensitized by different Ru(II) complexes in aqueous 0.1 M Na₂SO₄ solution containing 10 mM EDTA under intermittent visible light (λ > 420 nm). Reproduced from Ref. 71 with permission. Copyright 2015 American Chemical Society.

showed that electrodes modified with **Ru-CH₃** or **Ru-H** generated anodic photocurrent upon visible illumination, while the **Ru-CF₃** electrode did not even at more positive potentials (Figure 17B). The photocurrent observed indeed originates from electron injection from the excited-state Ru(II) photosensitizer molecules into the conduction band of the niobate nanosheet.

The oxidation potential of the ³MLCT excited-state of the three Ru(II) complexes (E_{ox}^*) undergoes a positive shift in the order of **Ru-CH₃**, **Ru-H**, and **Ru-CF₃** (see Figure 17A). This means that the electron injection efficiency decreases in the same order, and could explain the low H₂ evolution activity of the **Ru-CF₃** system both in the photocatalytic reaction and the photoelectrochemical measurement. The E_{CB} of HCa₂Nb₃O₁₀ nanosheets was estimated to be -1.13 V (vs. Ag/AgNO₃), which is more positive than or very close to the E_{ox}^* values of **Ru-CH₃** and **Ru-H** (-1.18 and -1.08 V, respectively). The E_{ox}^* value of **Ru-CF₃** ($E_{ox}^* = -0.67$ V vs. Ag/AgNO₃) is much more positive than those of **Ru-CH₃** and **Ru-H** (-1.18 and -1.08 V, respectively). The E_{CB} of HCa₂Nb₃O₁₀ nanosheets was estimated to be -1.13 V (vs. Ag/AgNO₃), which is more positive than or very close to the E_{ox}^* values of **Ru-CH₃** and **Ru-H**, enabling electron injection from the ³MLCT excited-state of these photosensitizers to restacked HCa₂Nb₃O₁₀ nanosheets and subsequent H₂ evolution.

3.5 Effect of Physicochemical Properties of Nanosheets.

The results of photocatalytic and photoelectrochemical reactions using different Ru(II) sensitizers that have different E_{ox}^* values indicated that the electron injection efficiency is definitely an important factor in determining the performance of sensitized photocatalysts for H₂ evolution. Similarly, the electron injection efficiency can be controlled by changing the E_{CB} of the semiconductor as well. As demonstrated earlier, restacked nanosheets of HCa_{2-x}Sr_xNb₃O₁₀ and HCa₂Nb_{3-y}Ta_yO₁₀ have different E_{CB} values, hence they are good candidates as components of sensitized H₂ evolution systems in order to further examine the effects of electron injection. HCa_{2-x}Sr_xNb₃O₁₀ nanosheets sensitized by **Ru-CH₃** exhibited activity for visible-light H₂ evolution, but the H₂ evolution rate was decreased with increasing concentration of Sr in HCa_{2-x}Sr_xNb₃O₁₀. Similarly, substitution of Nb in HCa₂Nb₃O₁₀ for Ta tended to decrease activity. Consequently, HCa₂Nb₃O₁₀ had the best performance as the building block for H₂ evolution

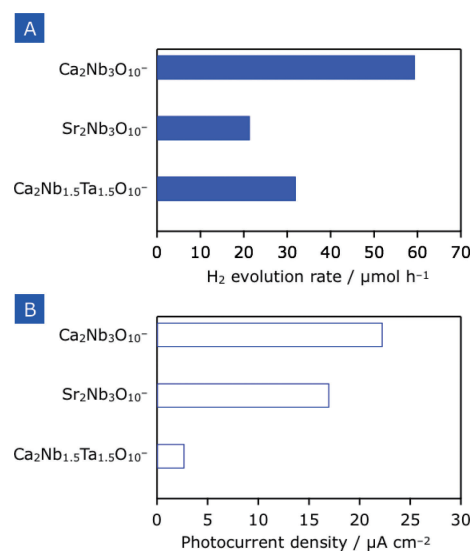


Figure 18. (A) H₂ evolution rate on 0.5 wt% Pt-loaded nanosheets sensitized by **Ru-CH₃** (8.0 μmol g⁻¹) under visible light (λ = 420 nm). Reaction conditions: catalyst, 25 mg; 10 mM aqueous EDTA solution, 100 mL; light source, 300 W xenon lamp with a band-pass filter. (B) Photocurrent density (at -0.55 V vs. Ag/AgCl) recorded using various nanosheet electrodes sensitized by **Ru-CH₃** in aqueous 0.1 M Na₂SO₄ solution containing 10 mM EDTA under visible light (λ > 420 nm). Reproduced from Ref. 71 with permission. Copyright 2015 American Chemical Society.

sensitized by **Ru-CH₃** with visible light among perovskite nanosheets examined, as shown in Figure 18A.⁷¹

Photoelectrochemical measurements indicated that the Ca- and Sr-substituted materials exhibited a similar level of photocurrent (~20 μA cm⁻²) to each other, while substitution of Nb for Ta led to a significant drop in photocurrent (Figure 18B). Increasing the Sr content in HCa_{2-x}Sr_xNb₃O₁₀ nanosheets shifts the E_{CB} value to more positive potential, while the E_{CB} value of HCa₂Nb_{3-y}Ta_yO₁₀ nanosheets shifts negatively with increasing Ta concentration (see Table 1), resulting in a reduced driving

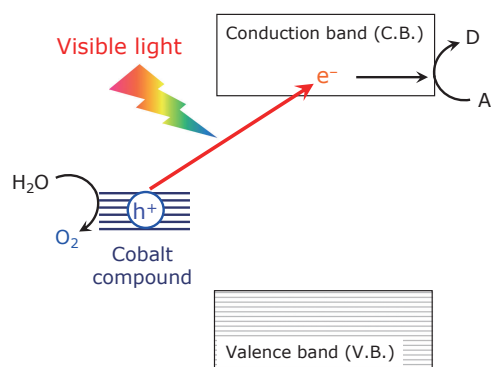


Figure 19. Water oxidation driven by charge transfer from $\text{Co}(\text{OH})_2$ (or Co_3O_4) to TiO_2 with water oxidation catalysis by $\text{Co}(\text{OH})_2$ (or Co_3O_4). Reproduced from Ref. 74 with permission. Copyright 2017 American Chemical Society.

force for electron injection. Therefore, the decrease in activity with increasing Ta content in $\text{HCa}_2\text{Nb}_{3-y}\text{Ta}_y\text{O}_{10}$ can be explained in terms of the reduced driving force for electron injection. We note, however, that the positively shifted E_{CB} of Sr-rich $\text{HCa}_{2-x}\text{Sr}_x\text{Nb}_3\text{O}_{10}$ had no positive impact on electron injection and the resulting H_2 evolution activity, compared to $\text{HCa}_2\text{Nb}_3\text{O}_{10}$. The decrease in activity with Sr substitution is probably due to the reduced driving force for proton reduction, which results from the positive shift of E_{CB} .

Another interesting result is that the dye-sensitized H_2 evolution activity was largely insensitive to the preparation conditions of the nanosheets (and their resulting crystallinity, specific surface area, and compositional homogeneity), as exemplified by the RuP^{2+} - $\text{HCa}_2\text{Nb}_3\text{O}_{10}$ system.³⁵ Results of steady-state emission spectroscopy indicated that the electron injection efficiency from the excited state RuP^{2+} to the $\text{HCa}_2\text{Nb}_3\text{O}_{10}$ nanosheet remained almost unchanged with respect to the nature of $\text{HCa}_2\text{Nb}_3\text{O}_{10}$. Therefore, the activity for sensitized H_2 production is primarily governed by the electron injection efficiency from the excited-state of the photosensitizer into the nanosheet. At the same time, a semiconductor material having E_{CB} suitable for both electron injection from the excited-state sensitizer and the reduction of protons is needed for efficient visible-light H_2 evolution.

For sensitized O_2 evolution, modification of a wide-gap metal oxide (which may include metal oxide nanosheets) with $\text{Co}(\text{OH})_2$ or Co_3O_4 nanoparticles has recently been shown to be effective.^{73–76} It is believed that the cobalt-modified semiconductors work by photoexcitation of electrons from the loaded cobalt species into the conduction band of the semiconductor, followed by catalytic oxidation of water that is promoted by electron-deficient cobalt species, as shown in Figure 19. However, a detailed investigation of metal oxide nanosheets as the component of the cobalt-sensitized O_2 evolution system has not been done yet, and will be performed as part of future work in our group.

4. Oxynitrides

4.1 Origin of Visible-Light-Absorption of Oxynitrides.

Besides dye-sensitization, valence band engineering of a metal oxide is another established means to make a visible-light-responsive photocatalyst. For this purpose, mixed anion com-

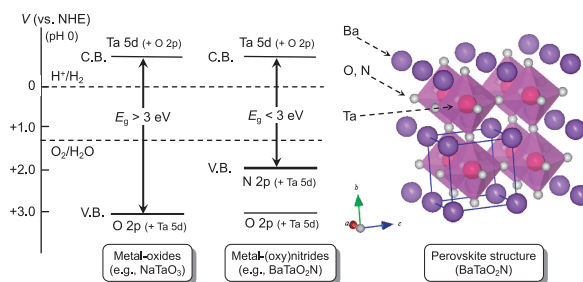


Figure 20. Schematic band structures of a metal oxide (NaTaO_3) and metal (oxy)nitride (BaTaO_2N) with perovskite structure. C.B., conduction band; V.B., valence band; E_g , bandgap energy; NHE, normal hydrogen electrode; V , potential. Reproduced from Ref. 78 with permission. Copyright 2011 Materials Research Society.

pounds that contain more than two different anions are key materials.⁷⁷ For example, because the N-2p orbital has a higher potential energy than O-2p, metal oxynitrides and nitrides are good candidates as narrow-gap photocatalysts.^{2,9,78} Figure 20 shows the schematic band structures of a metal oxide (NaTaO_3) and oxynitride (BaTaO_2N), both of which have the same perovskite structure. The valence band maximum for NaTaO_3 consists of O-2p orbitals, while the hybridized N-2p and O-2p orbitals are the main contributors to form the upper part of the valence band of BaTaO_2N , as revealed by density functional theory calculations. The valence band maximum of the oxynitride is located at higher potential energy than that of the corresponding oxide due to the contribution of N-2p orbitals, making the band gap sufficiently small to respond to visible light (<3 eV) with no significant influence on the conduction band minimum.²

In contrast to metal oxide systems shown earlier, oxynitride nanosheets are very rare. The main reason is the lack of layered oxynitrides that can undergo exfoliation. Alternatively, nitrogen-doped layered metal oxides have been reported.^{79–91} Some of them can transform into nanosheets, which exhibit visible-light photocatalytic activities.^{84–87} In the following sections, recent progress on oxynitride-type materials (including nitrogen-doped metal oxides) developed by the authors' group is described, focusing on nanosheets and related materials.

4.2 KTiNbO_5 -Type Layered Oxides and Their Nanosheets as Precursors of Oxynitride Photocatalysts Exhibiting Strong Absorption in Visible Light Region.

One of the most serious problems in nitrogen-doping is the charge imbalance caused by the substitution of O^{2-} in the host oxide for N^{3-} , which limits the nitrogen concentration in the doped metal oxide host to low levels. This is obviously unfavorable for visible-light absorption.^{92,93} Nitridation of a metal oxide is typically performed by heating the oxide under a flow of NH_3 gas at temperatures higher than 773 K.^{94,95} Nitridation at higher temperatures increases the reactivity of NH_3 with the oxide, producing an oxynitride that contains more nitrogen. At the same time, however, high-temperature nitridation inevitably causes the formation of thermally stable byproduct phases and/or reduced metal species, which are generally unfavorable for heterogeneous photocatalysis.⁹ It is therefore generally difficult to obtain a nitrogen-doped metal oxide that possesses sufficient

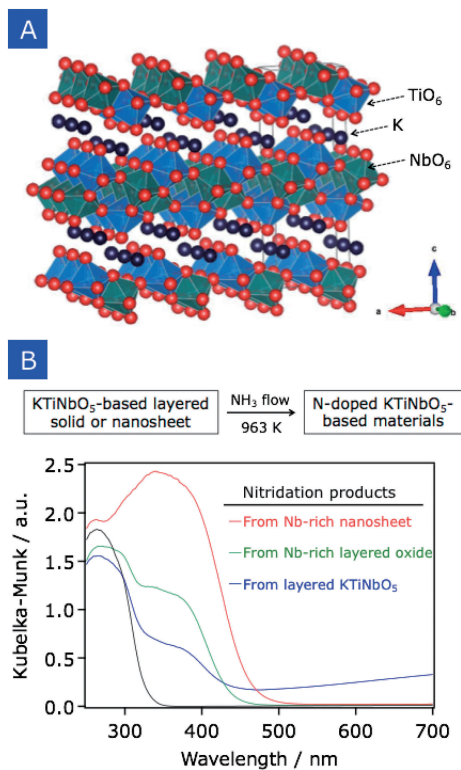


Figure 21. (A) Crystal structure of layered KTiNbO₅. (B) UV-visible DRS of nitrided KTiNbO₅ materials. Reproduced from Ref. 98 with permission. Copyright 2018 American Chemical Society.

visible-light absorption. Transient absorption spectroscopy also revealed that the charge imbalance in a nitrogen-doped metal oxide can lead to the formation of oxygen vacancies, which produce trap states of photogenerated charge carriers, resulting in lower photocatalytic activity.^{96,97}

An effective route to synthesize nitrogen-doped metal oxides using KTiNbO₅ was developed.⁹⁸ As shown in Figure 21A, KTiNbO₅ consists of TiNbO₅⁻ polyanion sheets interleaved with K⁺ cations for charge compensation,⁹⁹ with controllable Ti/Nb ratios (to a certain extent) that can form nonstoichiometric phases while maintaining the original crystal structure of the compound.¹⁰⁰ The use of a Nb-rich phase as the oxide precursor led to improved nitrogen-doping; that is, the nitrided material obtained from the Nb-rich precursor shows more pronounced visible light absorption than that derived from a stoichiometric precursor (Figure 21B). This improved nitrogen doping is most likely due to the excess positive charge of the Nb-rich precursor, which compensates the negative charge resulting from O²⁻/N³⁻ exchange during thermal ammonolysis with NH₃ gas.

KTiNbO₅ can be exfoliated into nanoscale sheets,¹⁰¹ which appears to be advantageous as an oxide precursor for nitridation, because a high surface area nanosheet material provides a better interface for NH₃ gas to access during nitridation. Actually, more effective nitrogen doping was realized using reassembled KTiNbO₅ nanosheets as precursors (Figure 21B). The more pronounced visible-light absorption of the nanosheet material resulted in enhanced photocatalytic activity for water oxidation under visible light.

4.3 Undoped Layered Oxynitride. As discussed above, undoped oxynitrides are obviously highly desirable. While a number of bulk-type (3D) oxynitrides have been reported, however, undoped oxynitride nanosheets have not been developed to date. There are only a few reports of undoped layered oxynitrides (e.g., Ba₂TaO₃N, Rb_{1.8}LaNb₂O_{6.3}N_{0.7}·1.0H₂O, and K_{1.6}Ca₂Nb₃O_{9.4}N_{0.6}·1.1H₂O),^{102–105} but accompanied by byproduct of thermally stable 3D perovskite phases in some cases. Therefore, the first step for producing undoped oxynitride nanosheets should be the synthesis of a phase-pure layered oxynitride.

Very recently, phase-pure Li₂LaTa₂O₆N with a layered perovskite structure was successfully prepared by thermal ammonolysis of a lithium-rich Li-La-Ta oxide precursor.¹⁰⁶ Li₂LaTa₂O₆N is a two-dimensional layered oxynitride that consists of double-layer [LaTa₂O₆N]²⁻ perovskite slabs interleaved with two Li cations (Figure 22A).¹⁰⁵ Scanning transmission electron microscopy (STEM) observations indicated high crystallinity of the synthesized Li₂LaTa₂O₆N (Figure 22B), which should be advantageous as a photocatalyst. In contrast to the oxide precursor that absorbs only UV light, Li₂LaTa₂O₆N is capable of absorbing visible light at wavelengths up to 500 nm, with an estimated band gap of ca. 2.5 eV (Figure 22C).

The photocatalytic activity of Li₂LaTa₂O₆N was examined with respect to CO₂ reduction using a Ru(II) binuclear complex (**RuRu'**) in the presence of TEOA as an electron donor. The hybrid system, **RuRu'**/Li₂LaTa₂O₆N, catalytically produced formate as the main product with high selectivity (97%) upon visible light irradiation ($\lambda > 400$ nm) according to step-wise photoexcitation of **RuRu'** and Li₂LaTa₂O₆N, as previously reported for several bulk type semiconductors (Figure 22D).^{107–111} While **RuRu'** is an efficient homogeneous photocatalyst for visible-light CO₂ reduction, it does not work under the same reaction conditions due to its low photo-oxidation ability.¹¹² Li₂LaTa₂O₆N alone also showed no activity because of the lack of an active site for CO₂ reduction. Importantly, the hybrid photocatalyst exhibited much higher photocatalytic performance than hybrids constructed with well-known 3D oxynitride perovskites (here CaTaO₂N and LaTaON₂). Transient absorption spectroscopy indicated that Li₂LaTa₂O₆N possesses lower density of mid-gap states that work as recombination centers of photogenerated electron/hole pairs, but a higher density of reactive electrons, as compared to CaTaO₂N and LaTaON₂. This should be responsible for the higher photocatalytic performance of this layered oxynitride.

5. Conclusion and Future Perspective

Metal oxide nanosheets designed as heterogeneous photocatalysts for water splitting have been highlighted, focusing on efforts made by the authors' groups over the past 10 years. Metal oxide nanosheets, such as Dion-Jacobson phase HCa₂Nb₃O₁₀, are highly active photocatalysts for H₂ evolution from aqueous methanol under band-gap irradiation. The sufficiently negative conduction band potential, high crystallinity, larger specific surface area and utilization of the interlayer space as reaction sites are important factors that lead to the high H₂ evolution activity of the nanosheets. By contrast, the O₂ evolution activity in the presence of IO₃⁻ as a reversible electron acceptor was found to be largely insensitive to the physico-

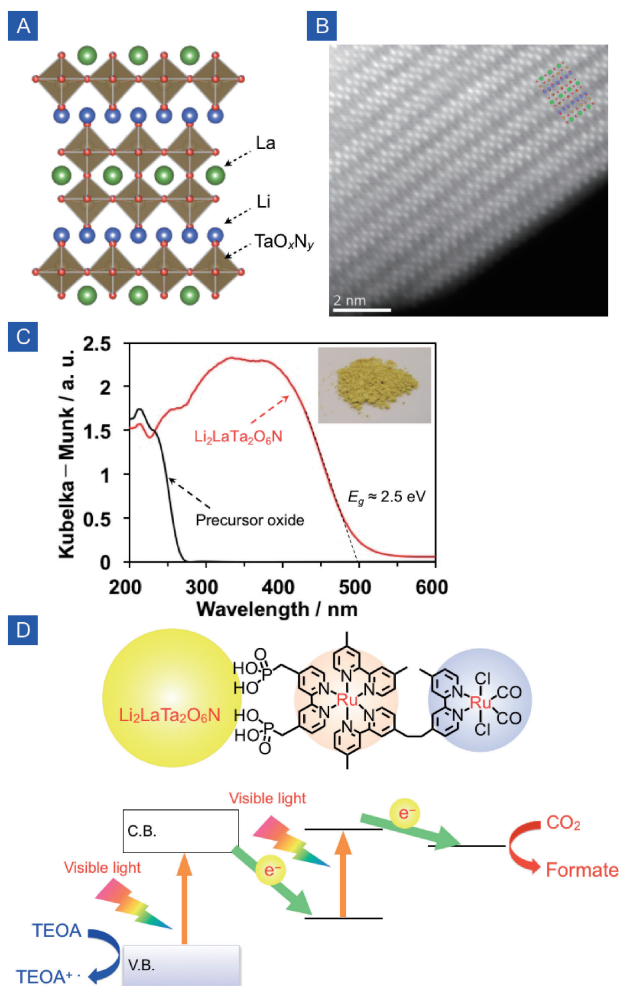


Figure 22. (A) Crystal structures of $\text{Li}_2\text{LaTa}_2\text{O}_6\text{N}$. (B) High-angle annular dark-field (HAADF)-STEM image of $\text{Li}_2\text{LaTa}_2\text{O}_6\text{N}$. The crystal structure of $\text{Li}_2\text{LaTa}_2\text{O}_6\text{N}$ is added, where blue marks: Li^+ , green: La^{3+} , brown: Ta^{5+} and red: $\text{O}^{2-}/\text{N}^{3-}$. (C) UV-visible DRS of $\text{Li}_2\text{LaTa}_2\text{O}_6\text{N}$ and its precursor. The inset shows a photograph of $\text{Li}_2\text{LaTa}_2\text{O}_6\text{N}$. (D) A Z-scheme CO_2 reduction system constructed with $\text{Li}_2\text{LaTa}_2\text{O}_6\text{N}$ and a Ru(II) binuclear complex that works under visible light to produce formate in the presence of TEOA as an electron donor. Reproduced from Ref. 106.

chemical properties of the nanosheets, but was influenced by the nature of reduction sites on them. Overall water splitting into H_2 and O_2 was demonstrated using restacked $\text{KCa}_2\text{Nb}_3\text{O}_{10}$ nanosheets in which the interlayer nanospace was modified with highly dispersed Pt nanoclusters <1 nm in size. Very recently, Nishioka et al. reported that electron doping (in other words, intentional formation of oxygen vacancies) into a metal oxide semiconductor, SrTiO_3 , improves its photocatalytic activity for the individual H_2/O_2 evolution reactions.¹¹³ In this case, the prolonged lifetime of photogenerated electrons and reinforced driving force for water oxidation, which are realized by electron doping, contribute to higher photocatalytic activities. This kind of electron doping (or defect-engineering) would be of interest for metal oxide nanosheets to further improve their photocatalytic activity.

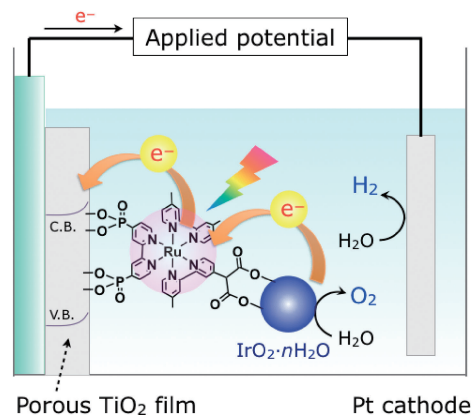


Figure 23. Schematic diagram of a water-splitting dye-sensitized solar cell that consists of porous TiO_2 film and a sensitizer-capped $\text{IrO}_2 \cdot n\text{H}_2\text{O}$ nanoparticle catalyst. Reproduced from Ref. 114 with permission. Copyright 2009 American Chemical Society.

Because metal oxide nanosheets are wide-gap semiconductors, most of them do not work under visible light. With modification by a suitable redox photosensitizer such as Ru(II) trisdiimine complexes, niobate nanoscrolls and nanosheets (further modified with Pt) become active for visible-light H_2 evolution from water containing EDTA as an electron donor. Some of them outperformed an analogous system that contained TiO_2 . The key to achieving efficient dye-sensitized H_2 evolution is to improve electron injection efficiency from the excited-state of the photosensitizer into nanosheet that has sufficiently negative conduction band potential for proton reduction. Mallouk et al. have applied dye-sensitized TiO_2 as the anode component of photoelectrochemical cells for visible-light water splitting (Figure 23).^{114,115} Abe et al. constructed a Z-scheme overall water splitting system using Pt-intercalated $\text{K}_4\text{Nb}_6\text{O}_{17}$ sensitized by a coumarin dye for H_2 evolution, a WO_3 -based photocatalyst for O_2 evolution, and an I_3^-/I^- redox couple.¹¹⁶ The findings of the studies on nanosheets made by the authors' groups will give useful information for further development of these systems.

In contrast to the facile dye-sensitization approach, the development of a visible-light-absorbing undoped metal oxide nanosheet material remains a challenge, due primarily to the difficulty in synthesizing a stable host layered material that can undergo exfoliation. Nevertheless, recent development in synthetic solid-state chemistry may enable us to produce such a new material. This possibility is currently under investigation in our groups.

The authors acknowledge their coworkers, whose names appear in the cited references. Acknowledgements are also extended to Grant-in-Aids for Young Scientists (A) (Nos. 25709078 and JP16H06130), for Scientific Research on Innovative Area (Nos. 25107512 and JP16H06441), and for Challenging Exploratory Research (No. JP15K14220). TEM acknowledges support from the Office of Basic Energy Sciences, Division of Chemical Sciences, Geosciences, and Energy Biosciences, Department of Energy, under contract DE-FG02-07ER15911. The work presented here was also supported in part

by a JSPS Fellowship for Young Scientists (No. 07J02395), the Noguchi Institute, the ENEOS Hydrogen Trust Fund and the “Chemical Conversion of Light Energy” PRESTO/Japan Science and Technology Agency (JST) program.

References

- 1 J. S. Lee, *Catal. Surv. Asia* **2005**, *9*, 217.
- 2 K. Maeda, K. Domen, *J. Phys. Chem. C* **2007**, *111*, 7851.
- 3 A. Kudo, Y. Miseki, *Chem. Soc. Rev.* **2009**, *38*, 253.
- 4 W. J. Youngblood, S.-H. A. Lee, K. Maeda, T. E. Mallouk, *Acc. Chem. Res.* **2009**, *42*, 1966.
- 5 R. Abe, *Bull. Chem. Soc. Jpn.* **2011**, *84*, 1000.
- 6 K. Maeda, *J. Photochem. Photobiol., C* **2011**, *12*, 237.
- 7 F. E. Osterloh, *Chem. Soc. Rev.* **2013**, *42*, 2294.
- 8 Y. Wang, X. Wang, M. Antonietti, *Angew. Chem., Int. Ed.* **2012**, *51*, 68.
- 9 K. Maeda, K. Domen, *Bull. Chem. Soc. Jpn.* **2016**, *89*, 627.
- 10 A. Miyoshi, S. Nishioka, K. Maeda, *Chem.—Eur. J.* **2018**, *24*, 18204.
- 11 B. A. Pinaud, J. D. Benck, L. C. Seitz, A. J. Forman, Z. Chen, T. G. Deutsch, B. D. James, K. N. Baum, G. N. Baum, S. Ardo, H. Wang, E. Miller, T. F. Jaramillo, *Energy Environ. Sci.* **2013**, *6*, 1983.
- 12 M. M. J. Treacy, S. B. Rice, A. J. Jacobson, J. T. Lewandowski, *Chem. Mater.* **1990**, *2*, 279.
- 13 S. W. Keller, H.-N. Kim, T. E. Mallouk, *J. Am. Chem. Soc.* **1994**, *116*, 8817.
- 14 T. Sasaki, M. Watanabe, H. Hashizume, H. Yamada, H. Nakazawa, *J. Am. Chem. Soc.* **1996**, *118*, 8329.
- 15 A. Takagaki, C. Tagusagawa, S. Hayashi, M. Hara, K. Domen, *Energy Environ. Sci.* **2010**, *3*, 82.
- 16 S. Ida, *Bull. Chem. Soc. Jpn.* **2015**, *88*, 1619.
- 17 H. Hata, S. Kudo, Y. Kobayashi, T. E. Mallouk, *J. Am. Chem. Soc.* **2007**, *129*, 3064.
- 18 S. Takagi, M. Eguchi, D. A. Tryk, H. Inoue, *J. Photochem. Photobiol., C* **2006**, *7*, 104.
- 19 M. Osada, T. Sasaki, *Adv. Mater.* **2012**, *24*, 210.
- 20 Y. Ebina, T. Sasaki, M. Harada, M. Watanabe, *Chem. Mater.* **2002**, *14*, 4390.
- 21 Y. Ebina, N. Sakai, T. Sasaki, *J. Phys. Chem. B* **2005**, *109*, 17212.
- 22 R. Uppuluri, A. S. Gupta, A. S. Rosas, T. E. Mallouk, *Chem. Soc. Rev.* **2018**, *47*, 2401.
- 23 H. Hata, Y. Kobayashi, V. Bojan, W. J. Youngblood, T. E. Mallouk, *Nano Lett.* **2008**, *8*, 794.
- 24 E. M. Sabio, M. Chi, N. D. Browning, F. E. Osterloh, *Langmuir* **2010**, *26*, 7254.
- 25 K. Domen, A. Kudo, A. Shinozaki, A. Tanaka, K. Maruya, T. Onishi, *J. Chem. Soc., Chem. Commun.* **1986**, 356.
- 26 A. Kudo, A. Tanaka, K. Domen, K. Maruya, K. Aika, T. Onishi, *J. Catal.* **1988**, *111*, 67.
- 27 O. C. Compton, E. C. Carroll, J. Y. Kim, D. S. Larsen, F. E. Osterloh, *J. Phys. Chem. C* **2007**, *111*, 14589.
- 28 O. C. Compton, C. H. Mullet, S. Chiang, F. E. Osterloh, *J. Phys. Chem. C* **2008**, *112*, 6202.
- 29 E. M. Sabio, R. L. Chamousis, N. D. Browning, F. E. Osterloh, *J. Phys. Chem. C* **2012**, *116*, 3161.
- 30 O. C. Compton, F. E. Osterloh, *J. Phys. Chem. C* **2009**, *113*, 479.
- 31 E. M. Sabio, R. L. Chamousis, N. D. Browning, F. E. Osterloh, *J. Phys. Chem. C* **2012**, *116*, 3161.
- 32 Y. Okamoto, S. Ida, J. Hyodo, H. Hagiwara, T. Ishihara, *J. Am. Chem. Soc.* **2011**, *133*, 18034.
- 33 M. R. Allen, A. Thibert, E. M. Sabio, N. D. Browning, D. S. Larsen, F. E. Osterloh, *Chem. Mater.* **2010**, *22*, 1220.
- 34 M. R. Waller, T. K. Townsend, J. Zhao, E. M. Sabio, R. L. Chamousis, N. D. Browning, F. E. Osterloh, *Chem. Mater.* **2012**, *24*, 698.
- 35 K. Maeda, M. Eguchi, W. J. Youngblood, T. E. Mallouk, *Chem. Mater.* **2009**, *21*, 3611.
- 36 M. Kakihana, M. Yoshimura, *Bull. Chem. Soc. Jpn.* **1999**, *72*, 1427.
- 37 A. Yamakata, H. Yeilin, M. Kawaguchi, T. Hisatomi, J. Kubota, Y. Sakata, K. Domen, *J. Photochem. Photobiol., A* **2015**, *313*, 168.
- 38 A. Yamakata, T. Ishibashi, H. Kato, A. Kudo, H. Onishi, *J. Phys. Chem. B* **2003**, *107*, 14383.
- 39 K. Maeda, M. Eguchi, T. Oshima, *Angew. Chem., Int. Ed.* **2014**, *53*, 13164.
- 40 Y. Miseki, H. Kato, A. Kudo, *Energy Environ. Sci.* **2009**, *2*, 306.
- 41 P. Xu, T. J. Milstein, T. E. Mallouk, *ACS Appl. Mater. Interfaces* **2016**, *8*, 11539.
- 42 K. Maeda, T. E. Mallouk, *J. Mater. Chem.* **2009**, *19*, 4813.
- 43 M. Machida, T. Mitsuyama, K. Ikeue, S. Matsushima, N. Arai, *J. Phys. Chem. B* **2005**, *109*, 7801.
- 44 K. Maeda, M. Eguchi, *Catal. Sci. Technol.* **2016**, *6*, 1064.
- 45 T. Oshima, O. Ishitani, K. Maeda, *Adv. Mater. Interfaces* **2014**, *1*, 1400131.
- 46 T. Oshima, T. Yokoi, M. Eguchi, K. Maeda, *Dalton Trans.* **2017**, *46*, 10594.
- 47 T. Oshima, M. Eguchi, K. Maeda, *ChemSusChem* **2016**, *9*, 396.
- 48 K. Maeda, R. Abe, K. Domen, *J. Phys. Chem. C* **2011**, *115*, 3057.
- 49 H. Suzuki, O. Tomita, M. Higashi, R. Abe, *Catal. Sci. Technol.* **2015**, *5*, 2640.
- 50 Y. Ebina, A. Tanaka, J. N. Kondo, K. Domen, *Chem. Mater.* **1996**, *8*, 2534.
- 51 Y. Ebina, K. Akatsuka, K. Fukuda, T. Sasaki, *Chem. Mater.* **2012**, *24*, 4201.
- 52 R. Ma, Y. Kobayashi, W. J. Youngblood, T. E. Mallouk, *J. Mater. Chem.* **2008**, *18*, 5982.
- 53 T. Oshima, D. Lu, O. Ishitani, K. Maeda, *Angew. Chem., Int. Ed.* **2015**, *54*, 2698.
- 54 R. Abe, K. Sayama, H. Arakawa, *Chem. Phys. Lett.* **2003**, *371*, 360.
- 55 N. Sakamoto, H. Ohtsuka, T. Ikeda, K. Maeda, D. Lu, M. Kanehara, K. Teramura, T. Teranishi, K. Domen, *Nanoscale* **2009**, *1*, 106.
- 56 T. Ikeda, A. Xiong, T. Yoshinaga, K. Maeda, K. Domen, T. Teranishi, *J. Phys. Chem. C* **2013**, *117*, 2467.
- 57 Y. Negishi, Y. Matsuura, R. Tomizawa, W. Kurashige, Y. Niihori, T. Takayama, A. Iwase, A. Kudo, *J. Phys. Chem. C* **2015**, *119*, 11224.
- 58 T. Oshima, D. Lu, K. Maeda, *ChemNanoMat* **2016**, *2*, 748.
- 59 D. E. Scaife, *Sol. Energy* **1980**, *25*, 41.
- 60 H. Gerischer, *Photochem. Photobiol.* **1972**, *16*, 243.
- 61 D. N. Furlong, D. Wells, H. F. Sasse, *J. Phys. Chem.* **1986**, *90*, 1107.
- 62 E. Bae, W. Choi, *J. Phys. Chem. B* **2006**, *110*, 14792.
- 63 A. Hagfeldt, G. Boschloo, L. Sun, L. Klöö, H. Pettersson, *Chem. Rev.* **2010**, *110*, 6595.

- 64 K. Maeda, M. Eguchi, W. J. Youngblood, T. E. Mallouk, *Chem. Mater.* **2008**, *20*, 6770.
- 65 G. B. Saupe, C. C. Waraksa, H.-N. Kim, Y. J. Han, D. M. Kaschak, D. M. Skinner, T. E. Mallouk, *Chem. Mater.* **2000**, *12*, 1556.
- 66 Here a possible current doubling effect was considered. Therefore, it is assumed that one H₂ molecule is produced by one photon.
- 67 K. Maeda, M. Eguchi, S.-H. A. Lee, W. J. Youngblood, H. Hata, T. E. Mallouk, *J. Phys. Chem. C* **2009**, *113*, 7962.
- 68 K. Hashimoto, M. Hiramoto, A. B. P. Lever, T. Sakata, *J. Phys. Chem.* **1988**, *92*, 1016.
- 69 K. Vinodgopal, X. Hua, R. L. Dahlgren, A. G. Lappin, L. K. Patterson, P. V. Kamat, *J. Phys. Chem.* **1995**, *99*, 10883.
- 70 A. Juris, V. Balzani, F. Barigelletti, S. Campagna, P. Belser, A. von Zelewsky, *Coord. Chem. Rev.* **1988**, *84*, 85.
- 71 K. Maeda, G. Sahara, M. Eguchi, O. Ishitani, *ACS Catal.* **2015**, *5*, 1700.
- 72 K. Izawa, T. Yamada, U. Unal, S. Ida, O. Altuntasoglu, M. Koinuma, Y. Matsumoto, *J. Phys. Chem. B* **2006**, *110*, 4645.
- 73 K. Maeda, K. Ishimaki, Y. Tokunaga, D. Lu, M. Eguchi, *Angew. Chem., Int. Ed.* **2016**, *55*, 8309.
- 74 K. Maeda, K. Ishimaki, M. Okazaki, T. Kanazawa, D. Lu, S. Nozawa, H. Kato, M. Kakihana, *ACS Appl. Mater. Interfaces* **2017**, *9*, 6114.
- 75 M. Okazaki, M. Eguchi, T. Uchiyama, D. Lu, H. Kato, Y. Uchimoto, M. Kakihana, K. Maeda, *Dalton Trans.* **2017**, *46*, 16959.
- 76 K. Ishimaki, T. Uchiyama, M. Okazaki, D. Lu, Y. Uchimoto, K. Maeda, *Bull. Chem. Soc. Jpn.* **2018**, *91*, 486.
- 77 H. Kageyama, K. Hayashi, K. Maeda, J. P. Attfield, Z. Hiroi, J. M. Rondinelli, K. R. Poeppelmeier, *Nat. Commun.* **2018**, *9*, 772.
- 78 K. Maeda, K. Domen, *MRS Bull.* **2011**, *36*, 25.
- 79 G. Liu, L. Wang, C. Sun, X. Yan, X. Wang, Z. Chen, S. C. Smith, H.-M. Cheng, G. Q. Lu, *Chem. Mater.* **2009**, *21*, 1266.
- 80 X. Zong, C. Sun, Z. Chen, A. Mukherji, H. Wu, J. Zou, S. C. Smith, G. Q. Lu, L. Wang, *Chem. Commun.* **2011**, *47*, 6293.
- 81 A. Mukherji, C. Sun, S. C. Smith, G. Q. Lu, L. Wang, *J. Phys. Chem. C* **2011**, *115*, 15674.
- 82 A. Mukherji, B. Seger, G. Q. Lu, L. Wang, *ACS Nano* **2011**, *5*, 3483.
- 83 S. Chen, J. Yang, C. Ding, R. Li, S. Jin, D. Wang, H. Han, F. Zhang, C. Li, *J. Mater. Chem. A* **2013**, *1*, 5651.
- 84 Y. Matsumoto, M. Koinuma, Y. Iwanaga, T. Sato, S. Ida, *J. Am. Chem. Soc.* **2009**, *131*, 6644.
- 85 S. Ida, Y. Okamoto, M. Matsuka, H. Hagiwara, T. Ishihara, *J. Am. Chem. Soc.* **2012**, *134*, 15773.
- 86 S. Ida, Y. Okamoto, H. Hagiwara, T. Ishihara, *Catalysts* **2013**, *3*, 1.
- 87 S. Ida, Y. Okamoto, S. Koga, H. Hagiwara, T. Ishihara, *RSC Adv.* **2013**, *3*, 11521.
- 88 C. Liu, L. Wu, J. Chen, J. Liang, C. Li, H. Ji, W. Hou, *Phys. Chem. Chem. Phys.* **2014**, *16*, 13409.
- 89 H. Suzuki, O. Tomita, M. Higashi, R. Abe, *J. Mater. Chem. A* **2016**, *4*, 14444.
- 90 K. Kawashima, M. Hojamberdiev, H. Wagata, K. Yubuta, K. Domen, K. Teshima, *ACS Sustainable Chem. Eng.* **2017**, *5*, 232.
- 91 X. Sun, Y. Mi, F. Jiao, X. Xu, *ACS Catal.* **2018**, *8*, 3209.
- 92 K. Nukumizu, J. Nunoshige, T. Takata, J. N. Kondo, M. Hara, H. Kobayashi, K. Domen, *Chem. Lett.* **2003**, *32*, 196.
- 93 K. Maeda, Y. Shimodaira, B. Lee, K. Teramura, D. Lu, H. Kobayashi, K. Domen, *J. Phys. Chem. C* **2007**, *111*, 18264.
- 94 S. G. Ebbinghaus, H.-P. Abicht, R. Dronskowski, T. Müller, A. Reller, A. Weidenkaff, *Prog. Solid State Chem.* **2009**, *37*, 173.
- 95 A. Fuertes, *Prog. Solid State Chem.* **2018**, *51*, 63.
- 96 A. Nakada, S. Nishioka, J. J. M. Vequizo, K. Muraoka, T. Kanazawa, A. Yamakata, S. Nozawa, H. Kumagai, S. Adachi, O. Ishitani, K. Maeda, *J. Mater. Chem. A* **2017**, *5*, 11710.
- 97 A. Miyoshi, J. J. M. Vequizo, S. Nishioka, Y. Kato, M. Yamamoto, S. Yamashita, T. Yokoi, A. Iwase, S. Nozawa, A. Yamakata, T. Yoshida, K. Kimoto, A. Kudo, K. Maeda, *Sustainable Energy Fuels* **2018**, *2*, 2025.
- 98 K. Maeda, Y. Tokunaga, K. Hibino, K. Fujii, H. Nakaki, T. Uchiyama, M. Eguchi, D. Lu, S. Ida, Y. Uchimoto, M. Yashima, *ACS Appl. Energy Mater.* **2018**, *1*, 1734.
- 99 A. D. Wadsley, *Acta Crystallogr.* **1964**, *17*, 623.
- 100 H. Rebbah, G. Desgardin, B. Raveau, *J. Solid State Chem.* **1980**, *31*, 321.
- 101 G. B. Saupe, T. E. Mallouk, W. Kim, R. H. Schmehl, *J. Phys. Chem. B* **1997**, *101*, 2508.
- 102 S. J. Clarke, K. A. Hardstone, C. W. Michie, M. J. Rosseinsky, *Chem. Mater.* **2002**, *14*, 2664.
- 103 J. A. Schottenfeld, A. J. Benesi, P. W. Stephens, G. Chen, P. C. Eklund, T. E. Mallouk, *J. Solid State Chem.* **2005**, *178*, 2313.
- 104 A. da Silva Maia, F. Cheviré, V. Demange, V. Bouquet, M. Pasturel, S. Députier, R. Lebullenger, M. Guilloux-Viry, F. Tessier, *Solid State Sci.* **2016**, *54*, 17.
- 105 M. Kaga, H. Kurachi, T. Asaka, B. Yue, J. Ye, K. Fukuda, *Powder Diffr.* **2011**, *26*, 4.
- 106 T. Oshima, T. Ichibha, K. S. Qin, K. Muraoka, J. J. M. Vequizo, K. Hibino, R. Kuriki, S. Yamashita, K. Hongo, T. Uchiyama, K. Fujii, D. Lu, R. Maezono, A. Yamakata, H. Kato, K. Kimoto, M. Yashima, Y. Uchimoto, M. Kakihana, O. Ishitani, H. Kageyama, K. Maeda, *Angew. Chem., Int. Ed.* **2018**, *57*, 8154.
- 107 K. Sekizawa, K. Maeda, K. Domen, K. Koike, O. Ishitani, *J. Am. Chem. Soc.* **2013**, *135*, 4596.
- 108 F. Yoshitomi, K. Sekizawa, K. Maeda, O. Ishitani, *ACS Appl. Mater. Interfaces* **2015**, *7*, 13092.
- 109 R. Kuriki, H. Matsunaga, T. Nakashima, K. Wada, A. Yamakata, O. Ishitani, K. Maeda, *J. Am. Chem. Soc.* **2016**, *138*, 5159.
- 110 K. Muraoka, H. Kumagai, M. Eguchi, O. Ishitani, K. Maeda, *Chem. Commun.* **2016**, *52*, 7886.
- 111 R. Kuriki, T. Ichibha, K. Hongo, D. Lu, R. Maezono, H. Kageyama, O. Ishitani, K. Oka, K. Maeda, *J. Am. Chem. Soc.* **2018**, *140*, 6648.
- 112 Y. Tamaki, O. Ishitani, *ACS Catal.* **2017**, *7*, 3394.
- 113 S. Nishioka, J. Hyodo, J. J. M. Vequizo, S. Yamashita, H. Kumagai, K. Kimoto, A. Yamakata, Y. Yamazaki, K. Maeda, *ACS Catal.* **2018**, *8*, 7190.
- 114 W. J. Youngblood, S.-H. A. Lee, Y. Kobayashi, E. A. Hernandez-Pagan, P. G. Hoertz, T. A. Moore, A. L. Moore, D. Gust, T. E. Mallouk, *J. Am. Chem. Soc.* **2009**, *131*, 926.
- 115 P. Xu, N. S. McCool, T. E. Mallouk, *Nano Today* **2017**, *14*, 42.
- 116 R. Abe, K. Shinmei, K. Hara, B. Ohtani, *Chem. Commun.* **2009**, 3577.